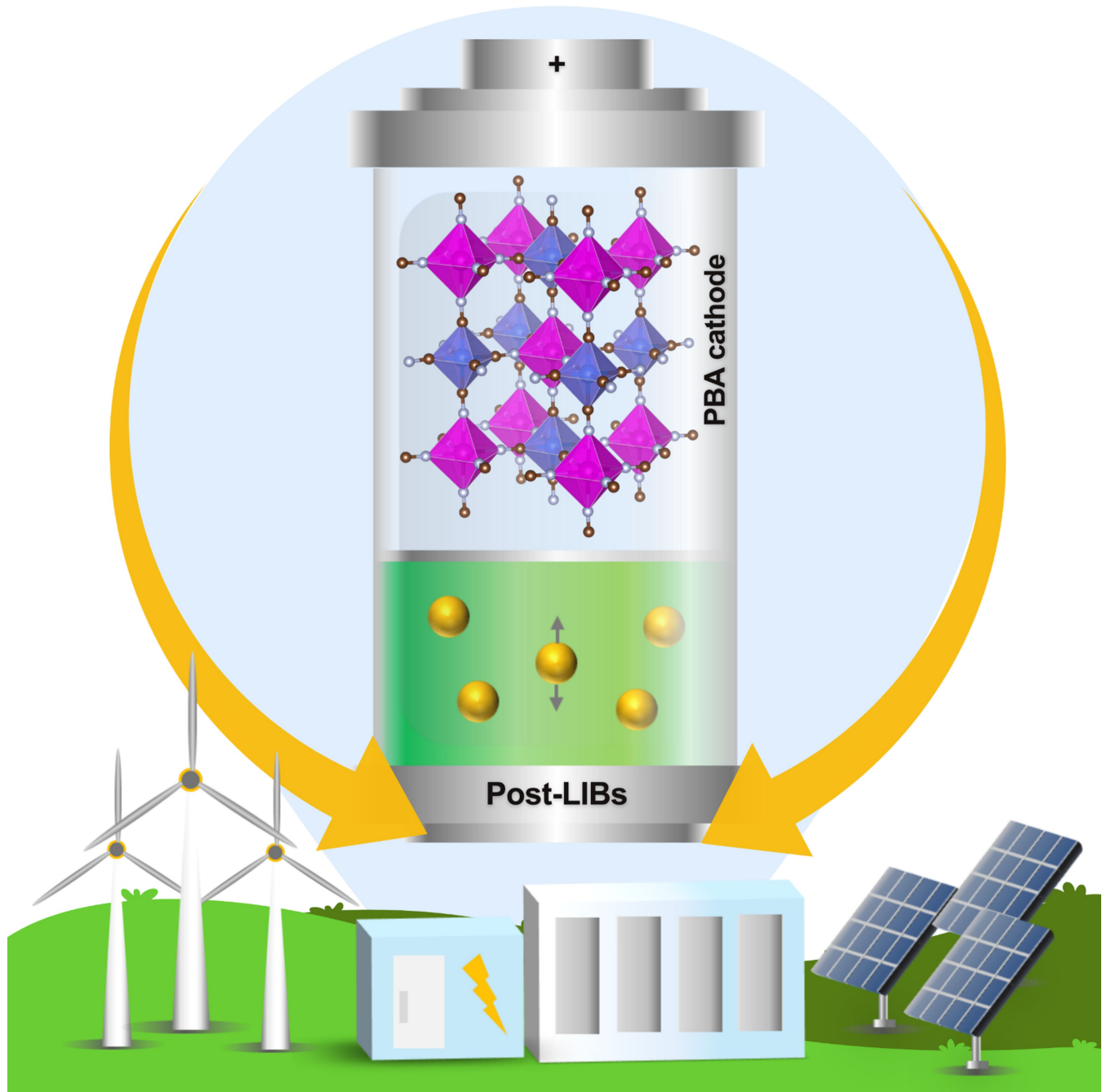


# Can Prussian Blue Analogues be Holy Grail for Advancing Post-Lithium Batteries?

Mecaelah S. Palaganas,<sup>[a, b]</sup> Jayson S. Garcia,<sup>[a, b, c]</sup> Giancarlo Dominador D. Sanglay,<sup>[a, c]</sup> Lora Monique E. Sapanta,<sup>[a, b, c]</sup> Lawrence A. Limjoco,<sup>[a, b]</sup> and Joey D. Ocon<sup>\*[a, b, c]</sup>



The recent classification of lithium as a critical raw material surged the research and development (R&D) of post-lithium batteries (PLBs). The larger cation charge carriers of these PLBs consequently entailed extensive materials R&D for battery components, especially cathode. Prussian Blue (PB) and its analogues (PBAs) have emerged as promising cathode materials for PLBs due to their desirable characteristics, including a three-dimensional open framework structure that facilitates fast ion diffusion for both monovalent ( $\text{Li}^+$ ,  $\text{Na}^+$ ,  $\text{K}^+$ ) and multivalent ( $\text{Mg}^{2+}$ ,  $\text{Ca}^{2+}$ ,  $\text{Zn}^{2+}$ ,  $\text{Al}^{3+}$ ) ions, stable framework structures, electrochemical tunability, availability of widely used precursors,

and ease of synthesis. Our comprehensive review reveals that several challenges are yet to be addressed in employing PBAs as cathode materials for PLBs, viz., vacancies, crystal water, side reactions, and conductivity issues. This review paper provides an exhaustive survey of material development, including the mitigation strategies of the challenges in employing PBAs as cathode materials for advancing PLBs (i.e., sodium-ion batteries (SIBs), potassium-ion batteries (KIBs), magnesium-ion batteries (MIBs), calcium-ion batteries (CIBs), zinc-ion batteries (ZIBs), aluminum-ion batteries (AIBs)) towards commercialization.

## 1. Introduction

Battery scientists have been consistent with their objectives for the past three decades: to decrease the weight and size of the battery (viz., increase the capacity per unit of battery), to increase cycle durability, and to maintain safety while minimizing cost.<sup>[1]</sup> Lithium's (Li) low atomic mass (6.94 u), high reducing nature [−3.04 V vs standard hydrogen electrode (SHE)] and wide voltage window with organic electrolytes make it ideal for higher energy density systems.<sup>[2]</sup> Furthermore, Li-ion's small atomic radius renders a high diffusion coefficient when used as a charge carrier, thereby establishing Li-ion batteries (LIBs) as the most predominant battery system in the market with high energy density and long cycle life (Figure 1a).

Motivations for battery research and development (R&D) have been consistent until 2020 when Li was officially classified as a critical raw material (Figure 1b)<sup>[3]</sup> due to its supply risk vis-à-vis uneven resource distribution (Figure 1c). This propels the R&D for post-Li battery (PLB) chemistry by replacing Li with less expensive and more abundant elements.<sup>[2,4]</sup>

Monovalent ion ( $\text{Na}^+$  and  $\text{K}^+$ ) batteries and multivalent ion ( $\text{Mg}^{2+}$ ,  $\text{Ca}^{2+}$ ,  $\text{Zn}^{2+}$ ,  $\text{Al}^{3+}$ ) batteries (MVIBs) both operate similarly to LIBs via a reversible ion intercalation mechanism. With  $\text{Na}^+$  and  $\text{K}^+$  being chemically similar to  $\text{Li}^+$  (i.e., Group 1A), it is anticipated that the development of monovalent ion batteries will follow the trajectory of LIBs<sup>[5]</sup> with sodium-ion batteries

(SIBs) already reaching commercial-scale technology maturity (Table 1). However, the larger ionic radii of  $\text{Na}^+$  (1.02 Å) and  $\text{K}^+$  (1.38 Å) cause sluggish reaction kinetics and repeated volume expansion/contraction of the electrodes during cycling, which results in inferior cycling stability.<sup>[6,7]</sup> Meanwhile, MVIBs hold great potential due to their multi-electron transfer capability,<sup>[2,8]</sup> which can result in higher gravimetric and volumetric energy density.<sup>[9]</sup> However, the slow desolvation at the cathode/electrolyte interface, caused by the strong interaction between the solvated ions and the solvent shell,<sup>[10–13]</sup> limits the MVIBs' performance.

Mechanism elucidation suggests a rational design of cathode materials that will permit the reversible intercalation of the larger ions throughout dis-/charging cycles if to develop high-performing PLBs. Various potential cathode materials have been prospected to this effect, including metal oxides and their derivatives, chalcogenides, polyanion compounds, carbon materials, and metal-organic frameworks (MOFs).<sup>[9,12–14]</sup>

MOFs are known to have tunable composition, structure, geometries, and morphologies (i.e., exceptional porosity) that can be beneficial to PLB development.<sup>[28,29]</sup> Particularly, Prussian Blue (PB) Analogues (PBAs) exhibit several advantages when used as cathode materials for monovalent ion batteries and MVIBs<sup>[30,31]</sup> due to: i) the 3D ion diffusion pathways in the open framework,<sup>[32]</sup> ii) the rigid structure of PBAs leading to relatively high cycling stability,<sup>[33]</sup> and iii) the rich combination of transition metals possible that allows for the tuning of the electrochemical properties of PBAs.<sup>[34]</sup> These structural features can explain the prominence of PBAs among various PLBs (Table 1).<sup>[35]</sup>

Herein, PBAs and their role in advancing PLBs (i.e., SIBs, potassium-ion batteries (KIBs), magnesium-ion batteries (MIBs), calcium-ion batteries (CIBs), zinc-ion batteries (ZIBs), aluminum-ion batteries (AIBs)) were systematically discussed and reviewed. The electrochemical performance (i.e., discharge capacity, cycling stability) of reported PBA-based monovalent ion batteries and MVIBs were collated and correlated to the structure and properties of the PBAs. This allowed the discussion of the different battery performance optimization techniques through the modification of the crystal structure, composition, morphology, and surface characteristics of PBAs. These established the foundation for evaluating PBAs as prominent cathode materials for the commercialization of PLBs. This review paper aims to provide a systematic and comprehensive survey of material development, including the mitigation strategies of the challenges in employing PBAs as cathode materials for advancing PLBs (i.e., sodium-ion batteries (SIBs), potassium-ion batteries (KIBs), magnesium-ion batteries (MIBs), calcium-ion batteries (CIBs), zinc-ion batteries (ZIBs), aluminum-ion batteries (AIBs)) towards commercialization.

[a] M. S. Palaganas, J. S. Garcia, G. D. D. Sanglay, L. M. E. Sapanta, Dr. L. A. Limjoco, Prof. J. D. Ocon  
Laboratory of Electrochemical Engineering (LEE), Department of Chemical Engineering,  
University of the Philippines Diliman  
Quezon City 1101, Philippines  
E-mail: lalimjoco.up.edu.ph  
E-mail: jdocon@up.edu.ph

[b] M. S. Palaganas, J. S. Garcia, L. M. E. Sapanta, Dr. L. A. Limjoco, Prof. J. D. Ocon  
DOST-NICER Advanced Batteries Center  
University of the Philippines Diliman  
Quezon City 1101, Philippines

[c] J. S. Garcia, G. D. D. Sanglay, L. M. E. Sapanta, Prof. J. D. Ocon  
Energy Engineering Program, National Graduate School of Engineering,  
College of Engineering  
University of the Philippines Diliman  
Quezon City 1101, Philippines

Supporting information for this article is available on the WWW under  
<https://doi.org/10.1002/batt.202400280>

hensive reference for the further development of PLBs, particularly employing PBAs, to compensate for the critical limitations of LIBs in realizing the indispensable function of batteries.

## 2. Prussian Blue Analogues

Since their discovery, PBAs have found versatile applications (Figure 2), including hydrogen storage,<sup>[36]</sup> batteries,<sup>[37,38]</sup> electrocatalysts,<sup>[39,40]</sup> biosensors,<sup>[41]</sup> electrochromic devices,<sup>[42]</sup> molecule-based magnets,<sup>[43]</sup> biomedical devices,<sup>[44]</sup> and barocaloric devices<sup>[45]</sup> due to their highly tunable physical and chemical properties. As more information regarding PBAs' electrochemical properties was discovered during the past decade, their application in energy storage, especially on PLB chemistries, has significantly increased. This section first discusses PBAs' structure, composition, and synthesis, followed by an elaboration of their performance when used as cathodes in various PLB systems (i.e., monovalent and multivalent batteries).

### 2.1. Structure and Composition

PBAs are hexacyanometallate compounds with the formula  $A_xM^a[M^b(CN)_6]_y\Box_{1-y}\cdot nH_2O$  ( $A$ =alkali or alkaline earth metal,  $M^a$ ,  $M^b$ =transition metals,  $\Box=M^b(CN)_6$  vacancies). The  $M^a$  and  $M^b$  ions are octahedrally coordinated to N and C atoms of the  $-C\equiv N-$  ligands, respectively, forming an open-framework structure which is capable of hosting A atoms (Figure 3a). The A atoms have preferable occupations in the interstitial lattice sites<sup>[46]</sup> according to their ionic radii and energy requirement.<sup>[47]</sup> For instance, while SIBs have four possible interstice sites for  $Na^+$  in the PBA structure ( $8c$ ,  $24d$ ,  $32f(n)$ , and  $32f(c)$ ), the  $24d$  site is the most favorable for  $Na^+$  occupation because it has the smallest free space suitable for its ionic size, resulting in lowest calculated binding energy ( $E_b$ ).<sup>[48]</sup>

PBAs are known to exist in three different phases, which are controlled by their composition and metal valence state: cubic (i.e.,  $Na_{1.53}Fe[Fe(CN)_6]\cdot 4.2H_2O$ ,  $Fm-3m$  space group,  $a=b=c=10.3711(1)\text{ \AA}$ ,  $\alpha=\beta=\gamma=90^\circ$ ),<sup>[49]</sup> monoclinic (i.e.,  $K_{1.99}Mn[Fe(CN)_6]_{0.94}\cdot 0.57H_2O$ , space group  $P21/n$ ,  $a=10.112$ ,  $b=7.328$ , and  $c=6.97\text{ \AA}$ ,  $\alpha=\gamma=90^\circ$   $\beta=90.06^\circ$ ),<sup>[50]</sup> and rhombohedral (i.e.,  $Na_{1.73}Fe[Fe(CN)_6]\cdot 3.8H_2O$ ,  $R-3$  space group,  $a=b=7.43079(1)\text{ \AA}$ ,  $c=17.6133(1)\text{ \AA}$ ,  $\alpha=\beta=90^\circ$ ,  $\gamma=120^\circ$ ).<sup>[49]</sup> Structural defects such as vacancies and crystal water are inherent in PBAs (Figure 3b) which are typically caused by the selection of  $M^a$  and  $M^b$  precursors with different valent states (tri-valent or bi-valent),



Mecaelah S. Palaganas is a Project Technical Specialist II at the Laboratory of Electrochemical Engineering, Department of Chemical Engineering, University of the Philippines (UP) Diliman. She is currently taking a Master of Science in Chemical Engineering at UP Diliman, where she also received her B. Sc. in Chemical Engineering (2019). Her primary research interests include developing novel cathode materials for battery applications.



Lora Monique E. Sapanta received her B. Sc. in Chemical Engineering from Mindanao State University-Illigan Institute of Technology in 2019. She is presently working as a researcher at the Laboratory of Electrochemical Engineering in the University of the Philippines Diliman where she is also taking up a Master's Degree in Energy Engineering. Her research interests embrace the development of cathode materials for next-generation batteries.



Jayson S. Garcia received his B.Sc. in Chemical Engineering (2020) from the University of the Philippines (UP) Diliman. He is currently pursuing his M.Sc. in Energy Engineering while working as a researcher at the Department of Chemical Engineering, UP Diliman. His work focuses on material design for next-generation batteries.



Dr. Lawrence A. Limjoco obtained his integrated MSc/PhD in Energy Science and Technology from the Myongji University, South Korea. He then worked as a Research Professor in the same institution. Currently, he is a Senior Lecturer of the Department of Chemical Engineering, UP Diliman. Dr. Limjoco also serves as the Project Chief Technical Specialist of the Project NextGen of the Advanced Batteries Center of the Philippines.



Giancarlo Dominador Sanglay is a Research Fellow II at the Laboratory of Electrochemical Engineering, Department of Chemical Engineering, University of the Philippines (UP) Diliman. He is currently taking up a straight PhD program in Energy Engineering at UP Diliman where he also obtained his B.Sc. in Materials Engineering (2020). His research interests include materials for next-generation batteries and electrocatalysts.



Prof. Joey D. Ocon is a Full Professor of the Department of Chemical Engineering in the University of the Philippines Diliman. He has BS (2008) and MS (2011) in Chemical Engineering from the same university and a Ph.D. in Environmental Science and Engineering (2015) from Gwangju Institute of Science and Technology South Korea. Prof. Ocon is also a Co-founder and Chief Science Officer of the battery technology start-up Nascent Battery Solutions Technologies.

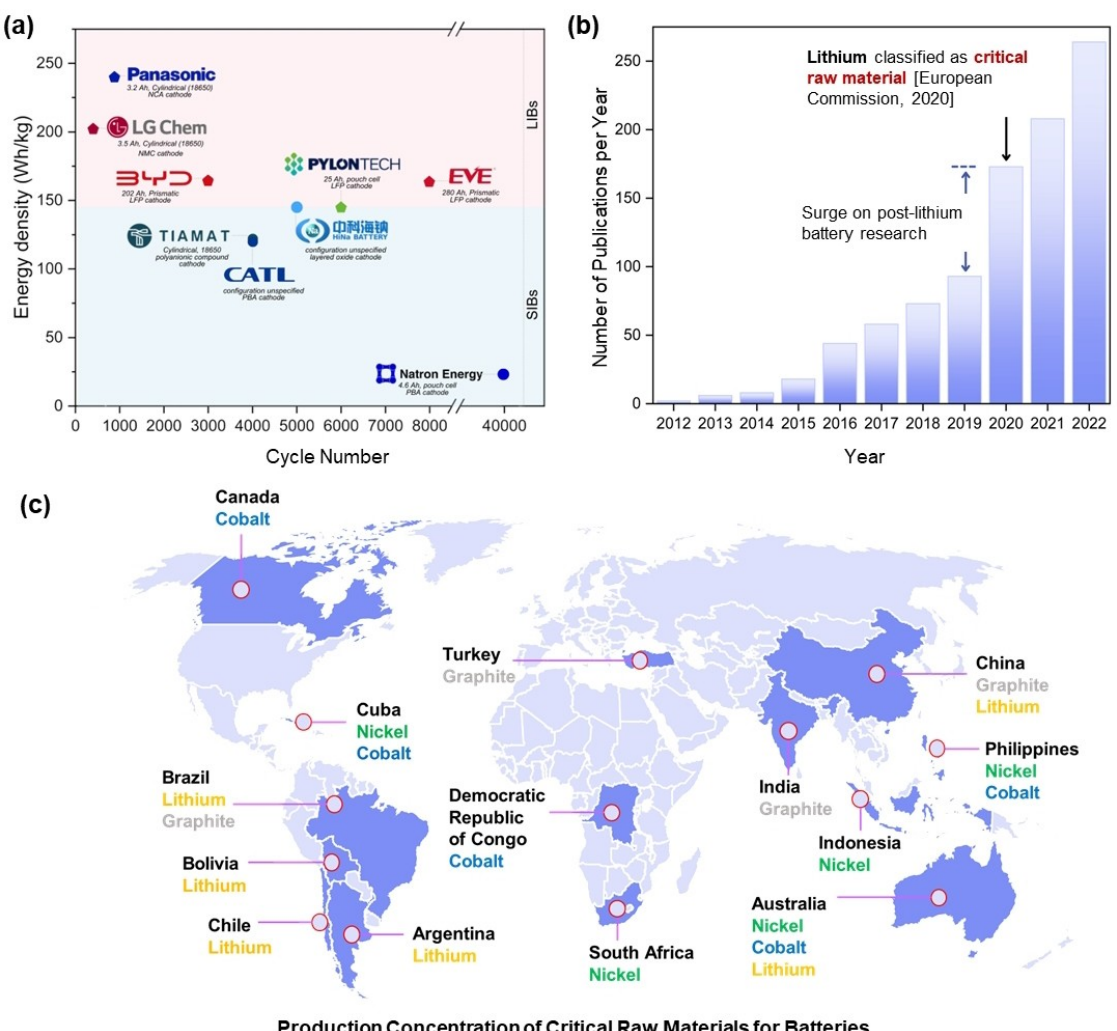


**Figure 1.** (a) Comparison of performance of commercially available LIBs and SIBs (details in Table S1). (b) Survey of the research publications per year on PLBs from 2012 to 2022 (keywords search: "post lithium battery"; "post lithium" + "monovalent"; "post lithium" + "multivalent"). (c) Production Concentration of Critical Raw Materials for Batteries. Reprinted from [15]. Copyright 2019, with permission from Elsevier.

leading to random vacant sites in the PBA structure that form to satisfy electrical neutrality. They appear in the A,  $[M^b(CN)_6]$ , and CN sites and adversely affect the electrochemical performance of PBAs by reducing the number of redox-active sites. This reduces the energy storage capacity and acts as a barrier to ion diffusion.<sup>[51]</sup> These vacancies also act as coordination sites for water, which occurs during crystal growth.<sup>[52]</sup> The two types of crystal water in PBAs are coordinated water, which occupies vacancies in the  $[M^b(CN)_6]$  cavity, and interstitial water, which occupies the 8c position left by A vacancies. Crystal water impedes ion diffusion, while interstitial water reduces the available sites for diffusing ions, thereby reducing the initial capacity.<sup>[51]</sup>

## 2.2. Synthesis

The composition and presence of defects in PBAs are sensitive to the choice of precursors and the reaction and growth

conditions. Thus, it is crucial to understand the synthesis of PBAs to control the structure and defect formation. Typical synthesis routes are coprecipitation, hydrothermal, ball-milling, and electrodeposition method (Figure S1). In coprecipitation, a  $M^a$ -salt aqueous solution is added dropwise to a  $[M^b(CN)_6]$  solution to prepare PBAs with defined metal compositions and nanostructures (Figure S1a).<sup>[59]</sup> The crystal nucleation and growth tend to be fast during coprecipitation due to the small dissolution equilibrium constant of PBAs, which results in nonuniform morphology.<sup>[59]</sup> To control the reaction rate, complexing agents are used.<sup>[60]</sup> Furthermore, alkali metal salts can also be added to the solution to increase alkali ion concentration and reduce defects.<sup>[61,62]</sup> The hydrothermal synthesis method typically uses a single transition metal precursor source reacted under high temperature and pressure. A  $[Fe(CN)_6]^{4-}$  precursor in an acidic medium decomposes into  $Fe^{3+}/Fe^{2+}$  ions that react with residual  $[Fe(CN)_6]^{4-}$  ions to form PBs (Figure S1b). This method is thus used in PBA synthesis composed of a single transition metal for  $M^a$  and  $M^b$ .<sup>[63]</sup> Varying

**Table 1.** Technology maturity level and cell performances of PLBs.

PLB Chemistry	Technology Maturity (Scale)		Electrochemical performances of commercial PLBs				Ref.	
	Laboratory	Commercial	Cell Chemistry	Energy Density (Wh kg <sup>-1</sup> )	Cycle Performance	Group		
SIB	✓	Cathode: Na <sub>x</sub> Mn <sub>y</sub> Fe(CN) <sub>6</sub> ·nH <sub>2</sub> O Anode: Na <sub>x</sub> Mn <sub>y</sub> Mn(CN) <sub>6</sub> ·nH <sub>2</sub> O Electrolyte: acetonitrile-based with proprietary sodium salt	23	> 40,000 cycles to 80% of the initial discharge capacity	Natron Energy	[16]		
		Cathode: Na <sub>x</sub> Mn[Fe(CN) <sub>6</sub> ]·nH <sub>2</sub> O Anode: hard carbon Electrolyte: non-aqueous electrolyte	100–130	98.6% after 500 cycles	Novasis Energies, Inc.	[17]		
		Cathode: Prussian white (PW) material Anode: hard carbon	160	capacity retention rate of more than 90% (at -20 °C)	Contemporary Amperex Technology (CATL)	[18]		
		Cathode: Na <sub>2</sub> Fe[Fe(CN) <sub>6</sub> ]·nH <sub>2</sub> O Anode: hard carbon	160	–	ALTRIS	[19]		
		Cathode: Na <sub>a</sub> Ni <sub>(1-x-y-z)</sub> Mn <sub>x</sub> Mg <sub>y</sub> Ti <sub>z</sub> O <sub>2</sub> Anode: hard carbon Electrolyte: 0.5 M NaPF <sub>6</sub> in aliphatic and cyclic carbonate solvents	120	400 cycles to 80% of the initial discharge capacity	Faradion Limited	[17]		
		Cathode: O <sub>3</sub> phase multi-composite layered cathode material Anode: soft carbon	145	≥ 4500 cycles @ 83% (2 C/2 C)	HiNa Battery	[20]		
		Cathode: Na <sub>3</sub> V <sub>2</sub> (PO <sub>4</sub> ) <sub>2</sub> F <sub>3</sub> Anode: hard carbon	122	3200 cycles at 2 C/5 C	Tiamat	[21,22]		
Electrochemical performances of representative laboratory-scale PLBs								
Cell Chemistry			Specific Capacity (mAh g <sup>-1</sup> )	Cycle Performance	Group	Ref.		
KIB	✓	Cathode: K <sub>1.90</sub> Ni <sub>0.5</sub> Fe <sub>0.5</sub> [Fe(CN) <sub>6</sub> ] <sub>0.89</sub> ·0.42H <sub>2</sub> O Anode: graphite Electrolyte: 1 M KPF <sub>6</sub> in ethylene carbonate (EC): diethyl carbonate (DEC): propylene carbonate (PC)	84.9 at 10 mA g <sup>-1</sup>	93.3% after 30 cycles at 50 mA g <sup>-1</sup>	Chong et al.	[23]		
		Cathode: K <sub>0.86</sub> Ni[Fe(CN) <sub>6</sub> ] <sub>0.95</sub> (H <sub>2</sub> O) <sub>0.766</sub> Anode: activated carbon pellet Electrolyte: 0.5 M Mg(ClO <sub>4</sub> ) <sub>2</sub> in acetonitrile (AN)	48.3 at 11.4 mA g <sup>-1</sup>	70% after 30 cycles at 11.4 mA g <sup>-1</sup>	Chae et al.	[24]		
MIB	✓	Cathode: K <sub>0.05</sub> Fe(III)[Fe(III)(CN) <sub>6</sub> ]·2.6H <sub>2</sub> O Anode: metallic zinc Electrolyte: 1.0 M Zn(CH <sub>3</sub> COO) <sub>2</sub> in choline acetate + 30 wt % H <sub>2</sub> O	122 at 10 mA g <sup>-1</sup>	94.3% after 10 cycles at 10 mA g <sup>-1</sup>	Liu et al.	[25]		
		Cathode: K <sub>0.02</sub> Cu[Fe(CN) <sub>6</sub> ] <sub>0.64</sub> ·9H <sub>2</sub> O Anode: polymerized polyaniline Electrolyte: 2.5 M Ca(NO <sub>3</sub> ) <sub>2</sub> in H <sub>2</sub> O	130 at 800 mA g <sup>-1</sup>	95% after 200 cycles at 0.8 A g <sup>-1</sup>	Adil et al.	[26]		
AIB	✓	Cathode: K <sub>0.02</sub> Ni <sub>1.45</sub> [Fe(CN) <sub>6</sub> ]·2.6H <sub>2</sub> O Anode: aluminum metal Electrolyte: 5 M aluminum trifluoromethanesulfonate (OTf) in H <sub>2</sub> O	46.5 at 20 mA g <sup>-1</sup>	~50% after 500 cycles	Gao et al.	[27]		

concentrations of reactants and solution pH have been shown to control the size of the PB crystals,<sup>[64]</sup> while varying the surfactant and water-to-surfactant ratio results in various PBA morphologies.<sup>[33]</sup>

In contrast to the discussed wet techniques, ball-milling is a solid-phase synthesis, allowing for a solvent-free approach. This method offers the advantage of avoiding direct contact between the PBA precursors and water. Ball-milling typically

grinds together alkali-transition metal-hexacyanide and transition metal salt powders under an inert atmosphere. The reactants are broken down by mechanical forces, and PBAs are formed by the interaction of the small particles (Figure S1c). For example, Na<sub>1.94</sub>Mn[Fe<sub>0.99</sub>(CN)<sub>6</sub>]<sub>0.95</sub>□<sub>0.05</sub>·1.92H<sub>2</sub>O has been synthesized via ball-milling with the amount of crystal water regulated based on the hydration of the precursors.<sup>[65]</sup>

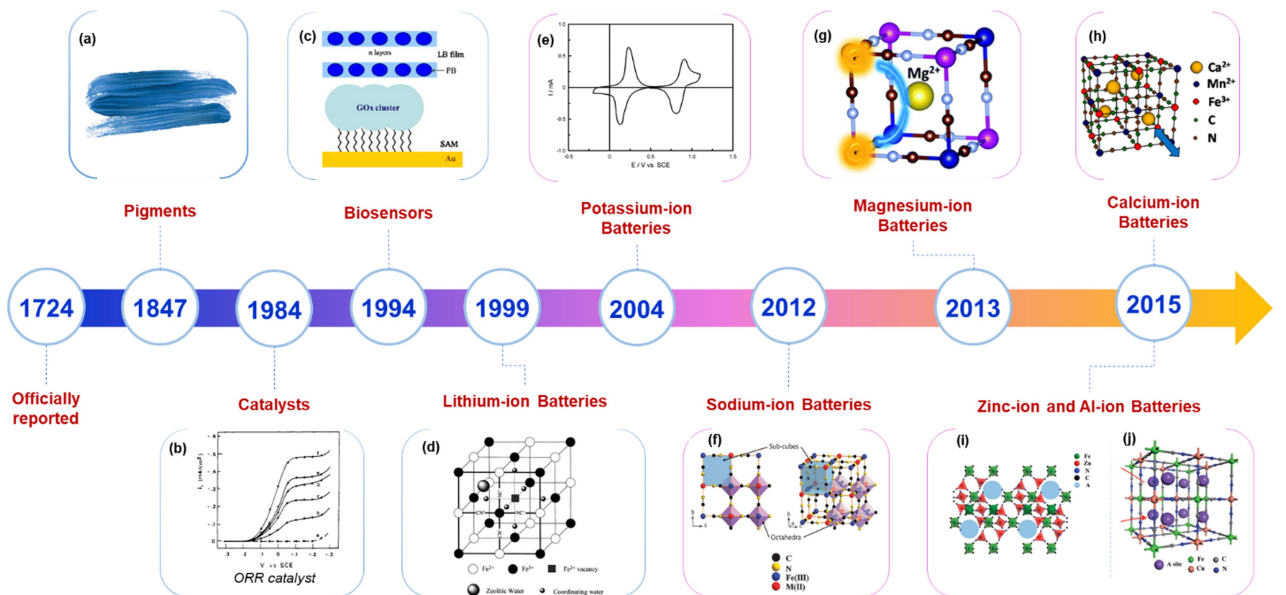


**Figure 2.** R&D timeline of PBAs and their applications in electrochemistry and energy storage. Applications from left to right: (a) Pigments. (b) Catalysts. Reprinted with permission from [40]. Copyright 1984, American Chemical Society. (c) Biosensors. Reprinted with permission from [41]. Copyright 2012, Elsevier. (d) LIBs. Reprinted with permission from [53]. Copyright 1999, Elsevier. (e) KIBs. Reprinted with permission from [30]. Copyright 2003, Elsevier. (f) SIBs. Reproduced with permission from [31]. Copyright 2012, The Royal Society of Chemistry. (g) MIBs. Reproduced with permission from [54]. Copyright 2013, The Royal Society of Chemistry. (h) CIIBs. Adapted with permission from [55]. Copyright 2015, American Chemical Society. (i) ZIBs. Reprinted with permission from [56]. Copyright 2014, Wiley-VCH Verlag GmbH & Co. KGaA, Weinheim. (j) AlIBs. Reproduced with permission from [57]. Copyright 2015, The Royal Society of Chemistry.

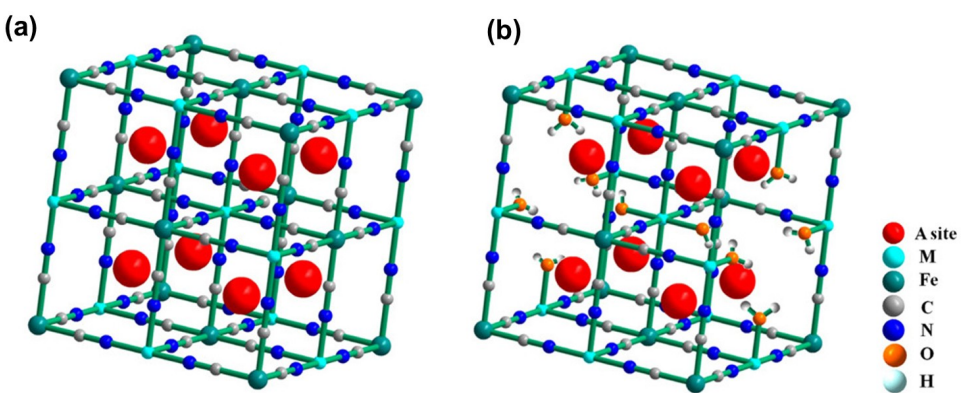


**Figure 3.** Crystal structures of PB framework: (a) ideal; (b) with vacancies and coordinated water defects. Adapted with permission from [58]. Copyright 2016, American Chemical Society.

Electrodeposition is a method that has been used to synthesize PBs by the electrochemical reaction of  $\text{Fe}^{3+}$  and  $[\text{Fe}(\text{CN})_6]^{4-}$  in an acidic medium (Figure S1d).  $\text{Fe}_4[\text{Fe}(\text{CN})_6]_3 \cdot \text{nH}_2\text{O}$  nanowires<sup>[66,67]</sup> and nanotubes<sup>[68]</sup> have been electrodeposited using a solution of  $\text{FeCl}_3$ ,  $\text{K}_3\text{Fe}(\text{CN})_6$ ,  $\text{KCl}$ , and  $\text{H}_3\text{BO}_4$ . This method unfortunately tends to use aqueous solutions due to the low solubility of ferrocyanide salts in organic solvents, leading to PBAs with vacancies and defects.<sup>[33]</sup>

### 2.3. Performance of PLBs with PBAs as Cathodes

The energy storage properties of PBAs are related to their composition and redox activity of the transition metals

involved. Depending on the activities of  $\text{M}^{\text{a}}$  and  $\text{M}^{\text{b}}$  in the applied potential window, PBAs are categorized as either single-electron (SE-PBA) transfer type (i.e.,  $\text{M}^{\text{b}} = \text{Fe}$ ,  $\text{M}^{\text{a}} = \text{Ni}, \text{Cu}$ ),<sup>[69]</sup> which has only one redox-active site capable of one-electron transfer process, and dual-electron (DE-PBA) transfer type (i.e.,  $\text{M}^{\text{b}} = \text{Fe}$ ,  $\text{M}^{\text{a}} = \text{Mn}, \text{Co}$ ),<sup>[70]</sup> which has two redox-active centers, capable of two-electron redox reaction. This explains the differences in the theoretical capacities of various PBAs with different compositions. (Table S2). Interestingly, in DE-PBAs,  $\text{M}^{\text{a}}$  typically has superior activity and a lower voltage plateau compared to  $\text{M}^{\text{b}}$ . A two-step voltage profile is observed for DE-PBAs, with each step corresponding to a redox reaction for each transition metal. The difference in behavior of the metal ions is due to differences in their electronic state.  $\text{M}^{\text{a}}$  is

coordinated to N, which is a weak ligand, leading to a high spin (HS) state, while M<sup>b</sup> is coordinated to C, a strong ligand, leading to a low spin (LS) state.<sup>[71,72]</sup>

### 2.3.1. Na<sup>+</sup> Ion Batteries (SIBs)

SIBs emerged as promising PLBs due to their inherent safety, low cost, and sustainable abundance of sodium resources.<sup>[73]</sup> While SIBs operate similarly to LIBs (via intercalation or “rocking chair” mechanism), SIBs exhibit significant differences in their chemical and electrochemical properties. For instance, SIBs have lower energy density due to their larger atomic weight (23 g mol<sup>-1</sup> for Na vs 7 g mol<sup>-1</sup> for Li) and due to their lower cell voltage due to the higher standard electrode potential of sodium (-2.71 V vs. SHE) compared with that of lithium (-3.02 V vs. SHE).<sup>[74,75]</sup> Additionally, the larger ionic radius of Na<sup>+</sup> (1.02 Å) compared to Li<sup>+</sup> (0.67 Å) significantly impacts the reaction kinetics and diffusion properties of SIBs. Calculations have revealed that the desolvation energy for Na<sup>+</sup> ions in various organic solvents was approximately 30% lower than that of Li<sup>+</sup> ions. This disparity in desolvation energy translates to a reduced charge transfer resistance and, consequently, improved electrode-electrolyte kinetics.<sup>[73,75]</sup> PBAs demonstrate promising electrochemical performance in the reversible intercalation of Na<sup>+</sup> ions, whether in aqueous or organic-based electrolytes (Table S3), which will be thoroughly covered in this section.

In a non-aqueous electrolyte, a Na-rich iron hexacyanoferrate (FeHCF) rhombohedral framework (Na<sub>1.73</sub>Fe[Fe(CN)<sub>6</sub>]<sub>0.92</sub>·3.8H<sub>2</sub>O) achieved 116 mAh g<sup>-1</sup> capacity (vs. Na) and retained ≈ 70 mAh g<sup>-1</sup> when subjected to a high current density of 2000 mA g<sup>-1</sup>. It also exhibits good cycling stability at 71% after 500 cycles (100 mA g<sup>-1</sup>) which is better than the Na-poor cubic framework (Na<sub>1.53</sub>Fe[Fe(CN)<sub>6</sub>]<sub>0.92</sub>·4.2H<sub>2</sub>O). This cathode was also tested in a full cell with a hard carbon anode, maintaining 78% capacity over 1000 cycles (1 C between 1.0–3.2 V) (Figure 4a–b).<sup>[49]</sup>

Manganese hexacyanoferrates (MnHCF) are also gaining attention as cathodes for SIBs due to their high energy density and resource abundance of Mn. Recently, Tang et al. (2020) prepared cubic MnHCF (Na<sub>1.38</sub>Mn[Fe(CN)<sub>6</sub>]<sub>0.92</sub>·2.57H<sub>2</sub>O) and monoclinic MnHCF (Na<sub>1.90</sub>Mn[Fe(CN)<sub>6</sub>]<sub>0.93</sub>·2.34H<sub>2</sub>O), with the former having 70% capacity retention for over 500 cycles (200 mA g<sup>-1</sup> vs Na), superior to the monoclinic structure (38% retention).<sup>[76]</sup> The reason behind this is that the cubic structure was able to maintain its cubic phase throughout the Na<sup>+</sup> de-/intercalation in the cathode (Figure 4c), while monoclinic MnHCF has multiple phase transitions (monoclinic↔cubic↔tetragonal), which leads to structural instability.

Cobalt hexacyanoferrates (CoHCF) are also capable of 2-Na redox reaction. Low-vacancy Na<sub>1.85</sub>Co[Fe(CN)<sub>6</sub>]<sub>0.99</sub>·2.5H<sub>2</sub>O nanocrystals displayed two voltage plateaus at +0.92 and +0.4 V for aqueous systems,<sup>[70]</sup> while thin films of Na<sub>1.6</sub>Co<sup>II</sup>[Fe<sup>II</sup>(CN)<sub>6</sub>]<sub>0.90</sub>·2.9H<sub>2</sub>O with ~400 nm crystalline grains exhibited discharge plateaus at +3.8 and +3.4 V in an organic-based electrolyte,<sup>[77]</sup> which correspond to the redox couples Fe<sup>2+</sup>/Fe<sup>3+</sup>

and Co<sup>2+</sup>/Co<sup>3+</sup>, respectively. Despite the promising performance (capacity up to 135 mAh g<sup>-1</sup>, CE ≥ 97%),<sup>[77]</sup> fewer studies have been reported compared to FeHCFs and MnHCFs due to the higher cost of cobalt.<sup>[38]</sup>

Various studies utilized copper hexacyanoferrate (CuHCF) as a cathode material for SIB application in both aqueous and non-aqueous electrolytes. Wang et al. worked on PBA-based composites for electrodes possessing high reversibility of Na<sup>+</sup> de-/intercalation processes. Their study proposed constructing a battery containing CuHCF (Na<sub>1.90</sub>Cu<sub>0.95</sub>[Fe(CN)<sub>6</sub>]<sub>0.92</sub>·1.9H<sub>2</sub>O) cathode and FeHCF (Na<sub>1.32</sub>Fe[Fe(CN)<sub>6</sub>]<sub>0.87</sub>·2.0H<sub>2</sub>O) anode with Ketjen Black (KB) in both diluted and concentrated solutions of NaNO<sub>3</sub> electrolyte (Figure 4d). The KB accelerated the nucleation process and reduced structural defects, which improved the crystallinity and electronic conductivity of the PBA-carbon composite electrodes. It was found that the electrolyte in a higher concentration improved the cycling stability of the CuHCF cathode, maintaining negligible capacity fading even after 250 cycles (Figure 4e).<sup>[78]</sup>

There are also numerous studies on PBA-based SIB full cells paired with organic anodes. One of these was a hybrid aqueous full cell developed by Kim et al. utilizing electrode materials that can be synthesized through facile procedures at low temperatures. The cathode used was KCo<sub>0.5</sub>Cu<sub>0.5</sub>Fe(CN)<sub>6</sub> and a carbonyl-based disodium naphthalenediimide (SNDI) salt (Figure 4f) was used as an anode with an aqueous electrolyte which exhibited a full cell potential of 1.1 V and a capacity of 34 mAh g<sup>-1</sup> at 20 C/10 C charging/discharging rates.<sup>[79]</sup>

### 2.3.2. K<sup>+</sup> Ion Batteries (KIBs)

KIBs are being touted as an emerging advancement in next-generation batteries due to their lower standard redox potential of -2.93 V vs. SHE than SIBs' -2.71 V vs. SHE.<sup>[80,81]</sup> This suggests KIBs to have greater theoretical values for output voltage and energy density than SIBs. Compared to LIBs and SIBs, the Stokes radius of solvated K<sup>+</sup> ions is smaller (Figure 5a), and their Lewis acidity is weaker, resulting in higher ionic conductivity and improved K<sup>+</sup> ions diffusion kinetics in electrolytes.<sup>[37,82]</sup> Moreover, for the same anodic limit of electrolyte decomposition (Figure 5b), it exhibits a wider voltage window compared to Li<sup>+</sup>.<sup>[83]</sup>

KIBs are limited though by structural instability during de-/intercalation due to the large radius of K<sup>+</sup> ions (1.38 Å), which consequently impairs the rate performance and energy density.<sup>[81,84,85]</sup> Thus, recent studies have focused on investigating suitable PBA-based cathode materials that provide structural integrity for the practical applications of KIBs (Table S4).

Jiang et al.<sup>[86]</sup> studied a novel K-rich PBA, potassium manganese ferrocyanide (K<sub>1.6</sub>Mn[Fe(CN)<sub>6</sub>]<sub>0.96</sub>·0.27H<sub>2</sub>O) with 1 M potassium bis(fluorosulfonyl)imide (KFSI) as the electrolyte in three different formulations EC:DEC, EC:DEC:fluoroethylene carbonate (FEC), PC:FEC. The charge transfer resistance increases most dramatically in the KFSI EC: DEC electrolyte, which supports that the other two electrolytes show a higher passivation layer conductivity due to FEC reduction. When

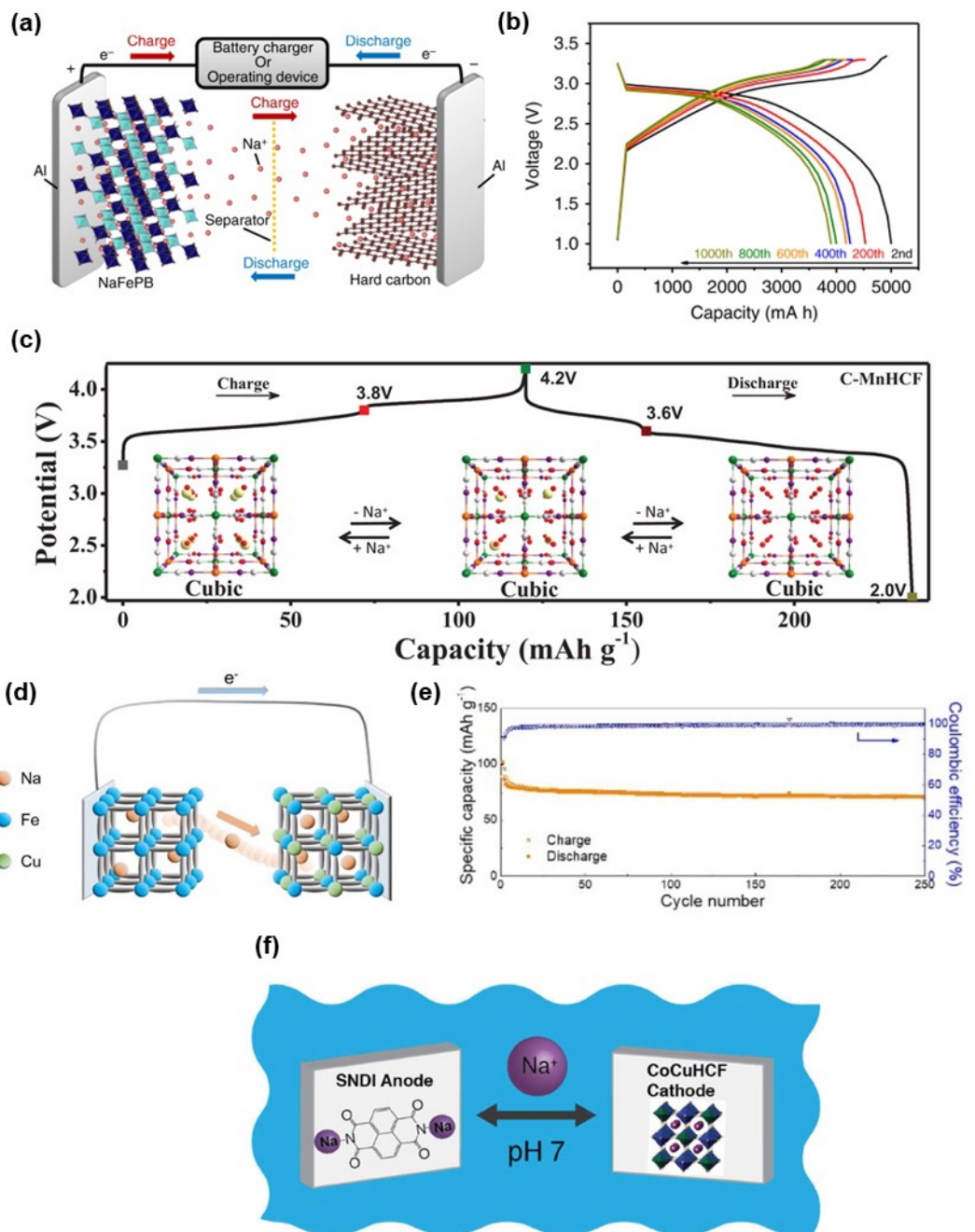


**Figure 4.** (a) Schematic illustration of a full-cell SIB with an FeHCF cathode and a hard carbon anode. (b) Corresponding charge-discharge curves for a full-cell SIB. Adapted with permission from [49]. Copyright 2020, Springer Nature. (c) Galvanostatic charge-discharge voltage curves and schematic illustration of structural evolution of cubic MnHCF ( $\text{Na}_{1.38}\text{Mn}[\text{Fe}(\text{CN})_6]_{0.92}\square_{0.08}\cdot2.57\text{H}_2\text{O}$ ). Reprinted from [76]. Copyright 2020, Wiley-VCH Verlag GmbH & Co. KGaA, Weinheim. (d) Schematic diagram of the working principle of an SIB with an FeHCF anode and CuHCF cathode. Reprinted with permission from [78]. Copyright 2019, Wiley-VCH Verlag GmbH & Co. KGaA, Weinheim. (e) Corresponding cycle performance of the CuHCF cathode. Reprinted with permission from [78]. Copyright 2019, Wiley-VCH Verlag GmbH & Co. KGaA, Weinheim. (f) Illustration of an SIB full cell with  $\text{KCo}_{0.5}\text{Cu}_{0.5}\text{Fe}(\text{CN})_6$  cathode and a disodium naphthalenediimide (SNDI) anode. Reprinted with permission from [79]. Copyright 2014, Wiley-VCH Verlag GmbH & Co. KGaA, Weinheim.

subjected to extended cycling, FEC-passivated cells can run up to 30 cycles since potassium metal was uniformly deposited in the active sites and suppressed dendritic growth in the  $K^+$  conducting passivation layer (Figure 5c).

Various approaches were devised to improve the electrochemical properties of potassium PB-based cathodes. One is the

dual stabilization strategy, which targets both the particles by enlarging the particle size and the cathode/electrolyte interface by reducing side reactions (Figure 5d).<sup>[37]</sup> Another is an enhanced synthesis route for potassium nickel hexacyanoferrate (NiHCF) ( $\text{K}_{1.86}\text{Ni}[\text{Fe}(\text{CN})_6]_{0.87}\square_{0.13}\cdot1.88\text{H}_2\text{O}$ ) via the electrostatic-assisted coprecipitation (ESAC) method, improving the crystal

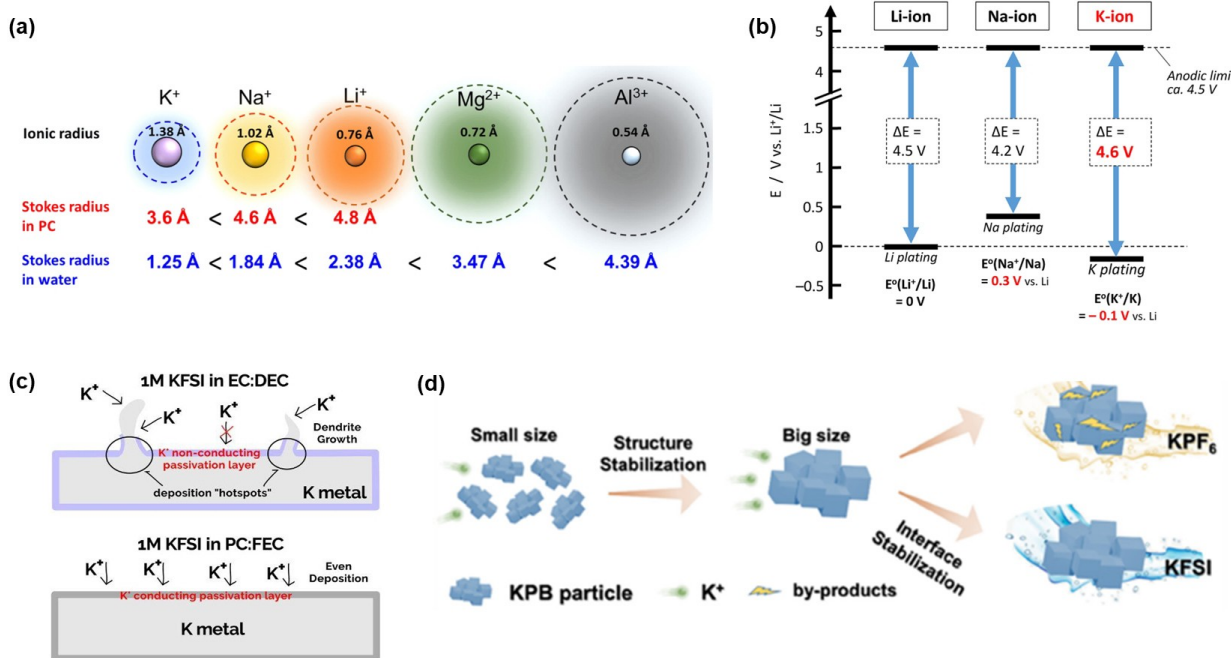


**Figure 5.** (a) Comparison of ionic radius and Stokes radius in PC and water for various ions. (b) Potential window comparison of Li<sup>+</sup>, Na<sup>+</sup>, and K<sup>+</sup> ions for non-aqueous electrolytes. Adapted with permission from [83]. Copyright 2020, American Chemical Society. (c) Illustration of potassium deposition in various electrolytes. Reprinted with permission from [86]. Copyright 2017, Wiley-VCH Verlag GmbH & Co. KGaA, Weinheim. (d) Dual-stabilization mechanism in potassium PB-based cathode structure and interface. Reprinted with permission from [37]. Copyright 2022, Elsevier.

structure under the influence of electrostatic repulsion. Despite the difference in approach, both of these methods attempt to further boost K<sup>+</sup> ion storage capacity, CE, and cyclic stability by mitigating potential structure defects and undesired side reactions and improving crystallinity and interfacial activity.<sup>[37,81]</sup>

### 2.3.3. MVIBs

While MVIBs are heavier and have larger radii than monovalent ion batteries, the former is regarded as promising PLBs, not only because of their natural abundance and low cost but also due to their multi-electron transfer capability during electrochemical ion de-/intercalation,<sup>[87]</sup> which can provide additional gravimetric and volumetric capacity.<sup>[10]</sup> However, the higher charge density of multivalent ions, which results in a stronger electrostatic interaction between the positive and negative atoms within the host framework, causes slow de-/intercalation kinetics in their host lattice<sup>[88]</sup> and poor cyclability.<sup>[89,90]</sup> In general, the intercalation of multivalent ions in their host lattice is more difficult than small monovalent ions due to their large ionic size (Figure 5a). In contrast to monovalent ion batteries, multivalent ions are expected to have a slower diffusion transport due to their stronger Lewis acidity and larger desolvation energy.<sup>[69]</sup> As such, an attractive host lattice for multivalent ions is one that has large interstitial sites for the reversible cation intercalation and has the ability to relieve the electrostatic repulsion of large ions<sup>[91]</sup> – all of which are met by PBA-based cathode materials. Recent research on this topic has focused on the use of PBAs such as CuHCF, CoHCF, NiHCF, and

FeHCF as cathode materials for MVIB applications. In this respect, the performance of the aforementioned PBAs studied in the literature, including but not limited to capacity, rate capability, cycling stability, and energy and power density, is discussed below, organized by the multivalent metal used.

#### 2.3.3.1. Mg<sup>2+</sup> Ion Batteries (MIBs)

MIBs are expected to be promising PLBs owing to magnesium's sufficient reserves, low price, inherent safety, better atmospheric stability, higher volumetric energy density, and low reduction potential (-2.37 V vs SHE). Also, Mg can deliver a two-electron redox reaction, delivering a high theoretical capacity of 3833 mAh cm<sup>-3</sup>.<sup>[92,93]</sup> Several PB frameworks have been studied for Mg<sup>2+</sup> intercalation in rechargeable batteries both for aqueous and organic systems (Table S5).

For instance, a CuHCF ( $K_{1.6}Cu[Fe(CN)_6]_{0.5} \cdot 1.4H_2O$ ) framework was synthesized by Yagi et al. and tested with an aqueous electrolyte (1.0 M MgSO<sub>4</sub>) and an organic 0.50 M magnesium bis(trifluoromethanesulfonyl) amide (Mg(TFSA)<sub>2</sub>) electrolyte. This cathode material delivered a discharge capacity of 40–60 mAh g<sup>-1</sup> for over 30 cycles at a 1 C rate in the 1.0 M MgSO<sub>4</sub> electrolyte, and the redox potential is around 3 V vs. Mg/Mg<sup>2+</sup> in both the organic and aqueous electrolytes. The high capacity in the aqueous electrolyte is due to the partial dehydration that occurred in Mg<sup>2+</sup> ions, which alleviated the electrostatic interaction of Mg<sup>2+</sup> ions with the framework constituents, resulting in fast diffusion of these ions (Figure 6a).<sup>[94]</sup> In contrast, a much lower charge-discharge capacity (2 mAh g<sup>-1</sup>) was

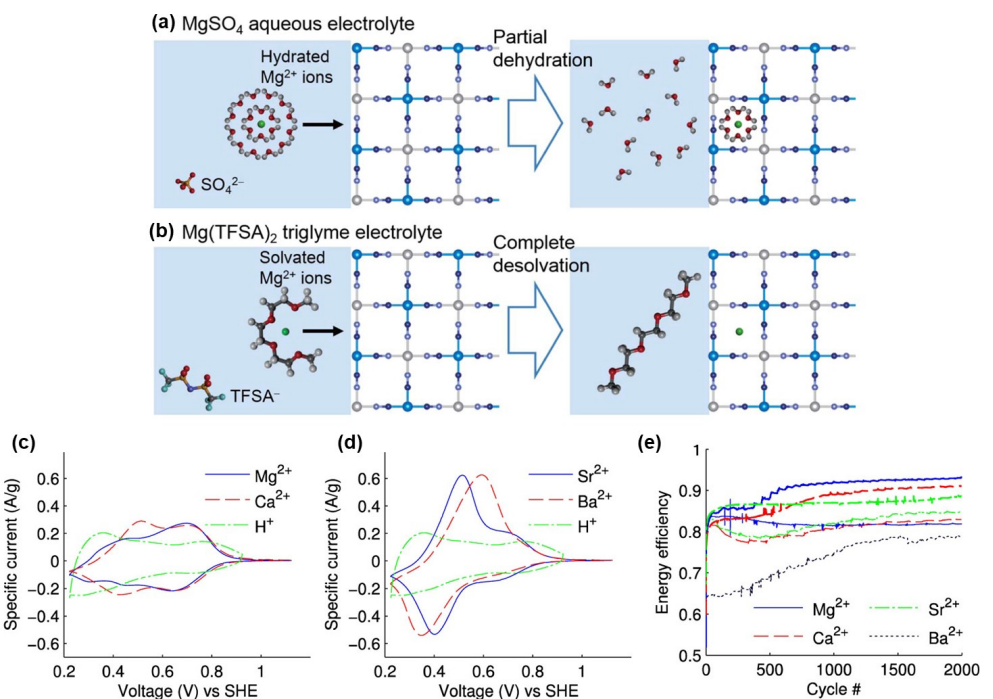


**Figure 6.** Illustration of the intercalation of Mg<sup>2+</sup> ions into the K<sub>1.6</sub>Cu[Fe(CN)]<sub>6</sub>·1.4H<sub>2</sub>O framework in (a) MgSO<sub>4</sub> aqueous electrolyte and (b) Mg(TFSA)<sub>2</sub> triglyme electrolyte. Adapted from [94]. Copyright 2015, The Author(s). Published by ECS. (c-d) Cyclic Voltammetry (CV) curves that demonstrate the reversible intercalation of Mg<sup>2+</sup>, Ca<sup>2+</sup>, Sr<sup>2+</sup>, and Ba<sup>2+</sup> ions in the NiHCF framework. (e) Energy efficiency of various divalent ions in a NiHCF framework (thick lines represent cells with additional Ni<sup>2+</sup> ions in the electrolyte). Adapted from [97]. Copyright 2013, American Chemical Society.

observed in the organic electrolyte due to a strong electrostatic interaction between the bare Mg<sup>2+</sup> ions and the cyano constituents of the K<sub>1.6</sub>Cu[Fe(CN)]<sub>6</sub>·1.4H<sub>2</sub>O framework. Because the Mg<sup>2+</sup> ions were completely desolvated, triglyme could not enter the PB framework due to its length (14.7 Å); thus, the shielding effect was not realized, resulting in a sluggish diffusion (Figure 6b).<sup>[94]</sup>

While Mg<sup>2+</sup> diffusion in PBAs is generally slow due to increased electrostatic interaction, it can be improved by incorporating a hydration sphere in the ion, which can provide shielding and improve kinetics in the PB cathode. Furthermore, dual-ion electrolytes involving other ions (Li<sup>+</sup>, Na<sup>+</sup>) can be used for co-intercalation, compensating for the slow kinetics of Mg<sup>2+</sup> ions.

### 2.3.3.2. Ca<sup>2+</sup> Ion Batteries (CIBs)

Calcium (Ca), the fifth most abundant element in the earth's crust (2500 times more abundant than Li and more abundant than Na and Mg), can serve as a low-cost substitute for LIBs. It also has a similar volumetric density (2072 mAh cm<sup>-3</sup>) as Li (2062 mAh cm<sup>-3</sup>) and has a lower charge density compared to other multivalent metal ions due to its larger ionic radius, resulting in better mobility of Ca<sup>2+</sup> ions in cathodes. It exhibits a similar deposition potential to Li (only 0.17 higher than Li and 0.5 lower than Mg), which could result in a higher operating voltage and energy density than Mg.<sup>[95,96]</sup> Furthermore, Ca is non-toxic, safe, and environmentally friendly, making it a

primary focus of research in multivalent rechargeable batteries.<sup>[96]</sup>

Reversible intercalation of divalent ions (Mg<sup>2+</sup>, Ca<sup>2+</sup>, Sr<sup>2+</sup>, Ba<sup>2+</sup>) was demonstrated by Wang et al.<sup>[97]</sup> in a KNiFe<sup>3+</sup>(CN)<sub>6</sub> cathode using 1 M Ca(NO<sub>3</sub>)<sub>2</sub> aqueous electrolyte (Figure 6c-d). For Ca<sup>2+</sup>, a capacity of 50 mAh g<sup>-1</sup> was achieved at a 0.2 C rate, and 53% of its initial capacity was retained after 2000 cycles at a 5 C rate. The huge drop and stabilization of capacity were caused by the saturation of the electrolyte with the dissolved Ni<sup>2+</sup> ions, which caused the electrode to stop dissolving. Adding 20 mM Ni<sup>2+</sup> before cycling significantly improved the specific capacity retention and energy efficiency not only for Ca<sup>2+</sup> but also for Mg<sup>2+</sup> and Sr<sup>2+</sup> (Figure 6e). The performance of Na<sub>0.45</sub>Ni[Fe(CN)]<sub>6</sub> host for Ca<sup>2+</sup> was also tested for organic electrolytes (0.2 M Ca(PF<sub>6</sub>)<sub>2</sub> in 3:7 EC:PC),<sup>[98,99]</sup> although substantial capacity fading was evident because the electrolyte is being consumed during cycling, caused by the lack of a good passivation layer. Nevertheless, the cell delivered a capacity of 60 mAh g<sup>-1</sup> at a current density of 10 mA g<sup>-1</sup>, and an intercalation voltage of 2.6 V vs Ca<sup>2+</sup>/Ca.<sup>[98]</sup> X-ray Diffraction (XRD) results show lattice expansion and contraction during discharging and charging, respectively. Even so, the overall expansion and contraction is 1%, indicating that Na<sub>0.45</sub>Ni[Fe(CN)]<sub>6</sub> is a stable framework that can intercalate Ca<sup>2+</sup> in nonaqueous electrolytes. A dehydrated K<sub>x</sub>NiFe(CN)<sub>6</sub>·nH<sub>2</sub>O cathode with KB additive was synthesized by Tojo et al. which gave a capacity of 40 mAh g<sup>-1</sup> and cycled reversibly 12 times in an organic electrolyte.<sup>[99]</sup> This structural stability is due to the strong atomic bonds and charge compensation of the metal framework.

Other cathode materials for calcium include FeHCF, MnHCF, CoHCF, and barium hexacyanoferrate ( $\text{BaHCF}$ )<sup>[100]</sup> – most of which use organic electrolytes (Table S6). For  $\text{CaCoFe}(\text{CN})_6$ , it has been demonstrated that the redox activity and capacity of CIBs were increased when water was added to the organic electrolyte (1 M  $\text{Ca}(\text{ClO}_4)_2 \cdot 6 \text{ H}_2\text{O}$  in AN + 2 ml  $\text{H}_2\text{O}$ )<sup>[101]</sup> due to the formation of a hydration sheath around the intercalating guest ions, which reduces their electrostatic interactions in the lattice.

### 2.3.3.3. $\text{Zn}^{2+}$ Ion Batteries (ZIBs)

Zinc (Zn) is the 23rd most abundant element in the earth's crust and the fourth most produced metal in the world, lowering its market price. It also has a high volumetric energy density, a high theoretical capacity, a low redox potential ( $-0.76 \text{ V}$  vs. SHE), and a high hydrogen evolution overpotential, making it suitable for use in aqueous solution. The smaller radius of the  $\text{Zn}^{2+}$  ion (0.74 Å) compared to that of the sodium ion (1.02 Å) is the primary reason for its fast kinetic behavior.<sup>[102]</sup> As a result, ZIBs are by far the most researched MVIBs (Table S7).

FeHCFs have been shown to be a good host lattice for  $\text{Zn}^{2+}$  in aqueous<sup>[103]</sup> and organic electrolytes.<sup>[25,104]</sup> Liu et al. developed a ZIB using a biodegradable, non-toxic, and environmentally friendly bio-ionic liquid electrolyte (1.0 M  $\text{Zn}(\text{CH}_3\text{COO})_2$ /(choline acetate + 30 wt% water), a  $\text{Fe}[\text{Fe}(\text{CN})_6] \cdot 2.5\text{H}_2\text{O}$  cathode, and a Zn metal anode. The intercalation of  $\text{Zn}^{2+}$  ion (Figure 7a) was confirmed by Fourier Transform Infrared Spectroscopy (FTIR) (Figure 7b) wherein the  $[\text{Fe}(\text{III})(\text{CN})_6]^{3-}$  and  $[\text{Fe}(\text{II})(\text{CN})_6]^{4-}$  peaks shift to a lower wavenumber for a fully discharged state. It was discovered that the high viscosity of ionic-liquid electrolytes, which restricts  $\text{Zn}^{2+}$  transport, causes the capacity to deterio-

rate with increasing current density. Nevertheless, even at a high discharge rate of  $60 \text{ mA g}^{-1}$ , the cell was still able to supply a capacity of roughly  $30 \text{ mAh g}^{-1}$  (Figure 7c). At  $10 \text{ mA g}^{-1}$ , the cell was able to achieve a reversible capacity of  $120 \text{ mAh g}^{-1}$  and a 99% CE.<sup>[25,104]</sup>

The ability of  $\text{NiFe}(\text{CN})_6$  to intercalate  $\text{Zn}^{2+}$  ions in non-aqueous electrolytes (0.5 M  $\text{Zn}(\text{TFSI})_2$  in AN) was also observed. Galvanostatic charge-discharge results show an initial capacity of  $50 \text{ mAh g}^{-1}$  at  $10 \text{ mA g}^{-1}$  and a voltage of  $1.2 \text{ V}$  vs.  $\text{Zn}/\text{Zn}^{2+}$ .<sup>[98]</sup> A higher potential range (vs.  $\text{Zn}^{2+}/\text{Zn}$ ) was achieved by using  $\text{CoFe}(\text{CN})_6$  (1.75 V)<sup>[105]</sup> and  $\text{Na}_2\text{MnFe}(\text{CN})_6$  (2 V),<sup>[106]</sup> cathode materials in aqueous electrolytes.

### 2.3.3.4. $\text{Al}^{3+}$ Ion Batteries (AIBs)

Aluminum (Al) metal, capable of a three-electron redox reaction, has a high volumetric capacity of  $8.04 \text{ Ah cm}^{-3}$ , a moderately high gravimetric capacity ( $2.98 \text{ Ah g}^{-1}$ ) and a high abundance in the Earth's crust (7.45%, 1200 times more than Li). As a result, considerable effort has been devoted to examining the chemistry and mechanism of rechargeable AIBs.<sup>[27]</sup>

While AIBs have a high theoretical capacity because of their small diameter and high valence state, a strong internal electrostatic force between  $\text{Al}^{3+}$  ions and the host lattice may hinder and limit  $\text{Al}^{3+}$  mobility, causing structural instability during de-/intercalation. This could result in rapid cathode degradation during cycling. Therefore, current research in AIBs is concentrated on developing cathode materials (Table S8) with stable interstitials and weak interaction with the  $\text{Al}^{3+}$  ion.<sup>[27]</sup>

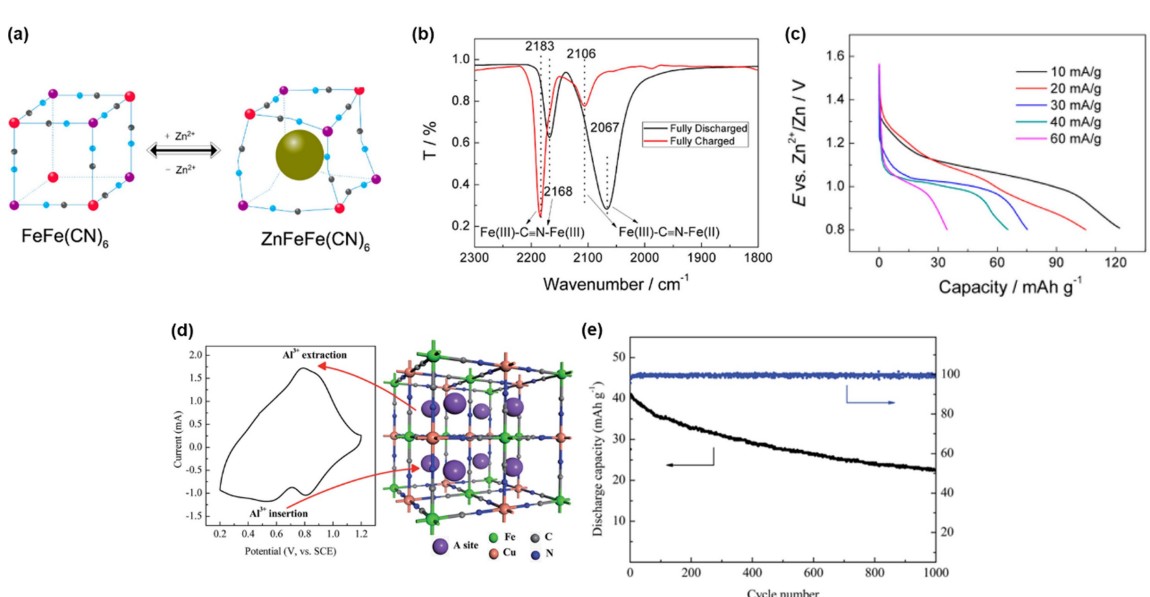


**Figure 7.** (a) Schematic illustration of the insertion of  $\text{Zn}^{2+}$  ions in FeHCF, (b) FTIR spectra of fully charged and discharged FeHCF, and (c) discharge profiles of FeHCF in ZIBs at different current densities. Adapted with permission from [25]. Copyright 2016, American Chemical Society. (d) CV curves of a CuHCF cathode in aqueous AIBs and the corresponding schematic diagram of  $\text{Al}^{3+}$  insertion/extraction. (e) Cycling performance of AIBs with  $\text{KCu}[\text{Fe}(\text{CN})_6] \cdot 8\text{H}_2\text{O}$  cathode in 0.5 M  $\text{Al}_2(\text{SO}_4)_3$  at  $400 \text{ mA g}^{-1}$ . Adapted from [57]. Copyright 2014, The Royal Society of Chemistry.

Reed et al. were the first to show an electrochemical cycling of aluminum ions in an organic electrolyte ( $\text{Al}(\text{OTF})_3$  in diglyme) and a  $\text{Cu}[\text{Fe}(\text{CN})_6]$  cathode.<sup>[107]</sup> A high initial discharge capacity of  $60 \text{ mAh g}^{-1}$  was obtained. However, the reversible capacity was only between 5 to  $14 \text{ mAh g}^{-1}$  and only lasted 10 cycles because of the destruction of the cathode material and the passivation of the anode.

Another study for ALBs in  $\text{KCu}[\text{Fe}(\text{CN})_6] \cdot 8\text{H}_2\text{O}$  cathode material was conducted using an aqueous electrolyte, 0.5 M  $\text{Al}_2(\text{SO}_4)_3$ . CV tests (Figure 7d) reveal that there is a two-step redox reaction occurring during  $\text{Al}^{3+}$  de-/intercalation, as characterized by two broad anodic peaks at 0.79 V and 0.85 V (vs. Standard Calomel Electrode, SCE) and two cathodic peaks at 0.81 V and 0.53 V (vs. SCE). The wide peaks indicate the limited mobility of  $\text{Al}^{3+}$  ions in the  $\text{KCu}[\text{Fe}(\text{CN})_6] \cdot 8\text{H}_2\text{O}$  framework due to the strong interaction of  $\text{Al}^{3+}$  and  $\text{C}\equiv\text{N}^-$  ligands, which also induces a steric effect. The reversible intercalation was still realized due to the shielding effect brought by the zeolitic water present in the structure. Cyclic performance tests were conducted, and the maximum discharge capacity at  $41 \text{ mAh g}^{-1}$  was gradually decreased by 54.9% after 1000 cycles due to the dissolution of  $\text{KCu}[\text{Fe}(\text{CN})_6] \cdot 8\text{H}_2\text{O}$  in the acidic electrolyte. Still, it was able to maintain a 100% CE for a number of cycles (Figure 7e), which demonstrates that the  $\text{KCu}[\text{Fe}(\text{CN})_6] \cdot 8\text{H}_2\text{O}$  cathode has a low side reaction in aqueous solutions.<sup>[57]</sup>

### 3. Performance Optimization Strategies for PBA-Based PLBs

Notwithstanding the strides made in the past years, the trajectory of PLBs employing PBAs as cathode material is still hampered by several challenges regarding the PBA's structure, properties, and performance that must be addressed.

#### 3.1. Crystal Structure Control

Synthesizing high-quality PBA crystals is instrumental to achieving structural stability and hence, better electrochemical performance. However, numerous PBAs show poor crystallinity and consequently, subpar electrochemical performances.<sup>[108]</sup> In PBAs, inherent crystal defects such as vacancies and crystal water content (including coordinated and interstitial water) are inevitably produced due to the rapid material synthesis brought by their low solubility constant ( $K = 3.3 \times 10^{-41}$ ),<sup>[109]</sup> which explains why its theoretical capacity is often not practically attainable. The presence of randomly distributed vacancies often leads to a breakdown of  $\text{M}_1\text{C}\equiv\text{N}\text{M}_2$  bridges, resulting in structural collapse and hindrance of ion transport during charge/discharge cycles.<sup>[110]</sup> Furthermore, the loss of  $\text{M}_1(\text{CN})_6$  octahedra,<sup>[111]</sup> which are typically taken up by coordinated and interstitial water, would result in vacancy-rich structures with large interstices. Because crystal water has a competitive relationship with metal ions, the increased water content in the lattice causes a reduced number of metal ions in the PBA unit

cell, consequently resulting in low specific capacity, low initial CE, and poor cycling performance.<sup>[33]</sup>

Phase transformations during the charging and discharging process also cause capacity fading over time. Particularly, the Jahn-Teller effect of  $\text{Mn}^{3+}$  causes structural deformation in MnHCFs, where a change in oxidation state ( $\text{Mn}^{2+} \rightarrow \text{Mn}^{3+}$ ,  $\text{Fe}^{2+} \rightarrow \text{Fe}^{3+}$ ) during metal de-/intercalation triggers a Mn–N equatorial distance contraction. As a result, significant volume changes in the order of 10–20% arise, which consequently deteriorates the cycle performance of PBA-based batteries.<sup>[112]</sup>

To combat the above issues and to further enhance the performance of PBAs as cathode materials for rechargeable batteries, it is imperative to employ various synthesis techniques that focus on controlling their crystal structure (i.e., crystal phase tuning, crystals with fewer vacancies and interstitial/coordinated water), as discussed in detail hereafter.

Rehman et al.<sup>[113]</sup> utilized a chelating agent-assisted coprecipitation method to fabricate low-defect, Na-rich NiHCF crystals for SIBs. In this sodium citrate-assisted process, the  $\text{Ni}^{2+}$  ions initially linked with citrate ions to form a nickel-citrate complex, which served as a buffer for the slow release of  $\text{Ni}^{2+}$ , preventing abrupt crystal growth and suppressing the aggregation of crystals. Ethylenediaminetetraacetic acid disodium (EDTA-2Na) was shown to have the same effect in the nucleation process of MnHCF.<sup>[114]</sup> The strong chelating ability of EDTA ( $K_{\text{stable}}[\text{Mn}-(\text{EDTA})]^{2-} = 10^{13.8}$ ) to  $\text{Mn}^{2+}$  slowed down the release of Mn ions, which decreased the nucleation rate and produced MnHCF with less crystal water content. In KIBs, an analogous chelating agent (EDTA-2 K) (Figure 8a)<sup>[115]</sup> resulted in a KFeHCF ( $K_{1.61}\text{Fe}[\text{Fe}(\text{CN})_6]_{0.88} \cdot 0.43\text{H}_2\text{O}$ ) framework with a better crystallinity and a higher K-ion diffusion coefficient than the product obtained without EDTA in the precursor.

The addition of surfactants such as polyvinylpyrrolidone (PVP) is another way to modulate the crystallinity of PBAs,<sup>[48,116]</sup> owing to their ability to selectively bind to crystal faces and inhibit crystal growth in other directions. In aqueous solutions, PVP forms a metastable micelle when it adsorbs on the surface of PBAs (Figure 8b). This weakens the attraction between  $\text{H}_2\text{O}$  and  $\text{C}\equiv\text{N}^-$  ligands, thereby reducing the interstitial water in the structure (Figure 8c).<sup>[117]</sup>

Incorporating excess salts such as NaCl and KCl in the precursors during the synthesis process<sup>[49]</sup> can also have a profound effect on the material's crystal structure. Li et al.<sup>[118]</sup> incorporated varying amounts of NaCl (0, 2, 7, and 21 g, and saturated) into the precursor solution for a one-step HCl-assisted hydrothermal synthesis. Upon increasing concentrations of NaCl, the XRD peak shifts towards smaller 2θ angles, as observed in the PB prepared in saturated NaCl, which exhibits a (200) peak at 2θ about 17.14°, compared to the pristine  $\text{Na}_{1+x}\text{Fe}[\text{Fe}(\text{CN})_6]$  with a (200) peak at 2θ about 17.46° (Figure 8d). This shift indicates an increase in interplanar distance and lattice parameters, which confirms that more  $\text{Na}^+$  ions enter into the cubic unit cell as the concentration of NaCl increases. As more  $\text{Na}^+$  ions enter the lattice, the  $\text{Fe}^{2+}/\text{Fe}^{3+}$  ratio approaches unity, implying that the amount of  $[\text{Fe}(\text{CN})_6]$  vacancy decreases. Consequently, the amount of coordinated

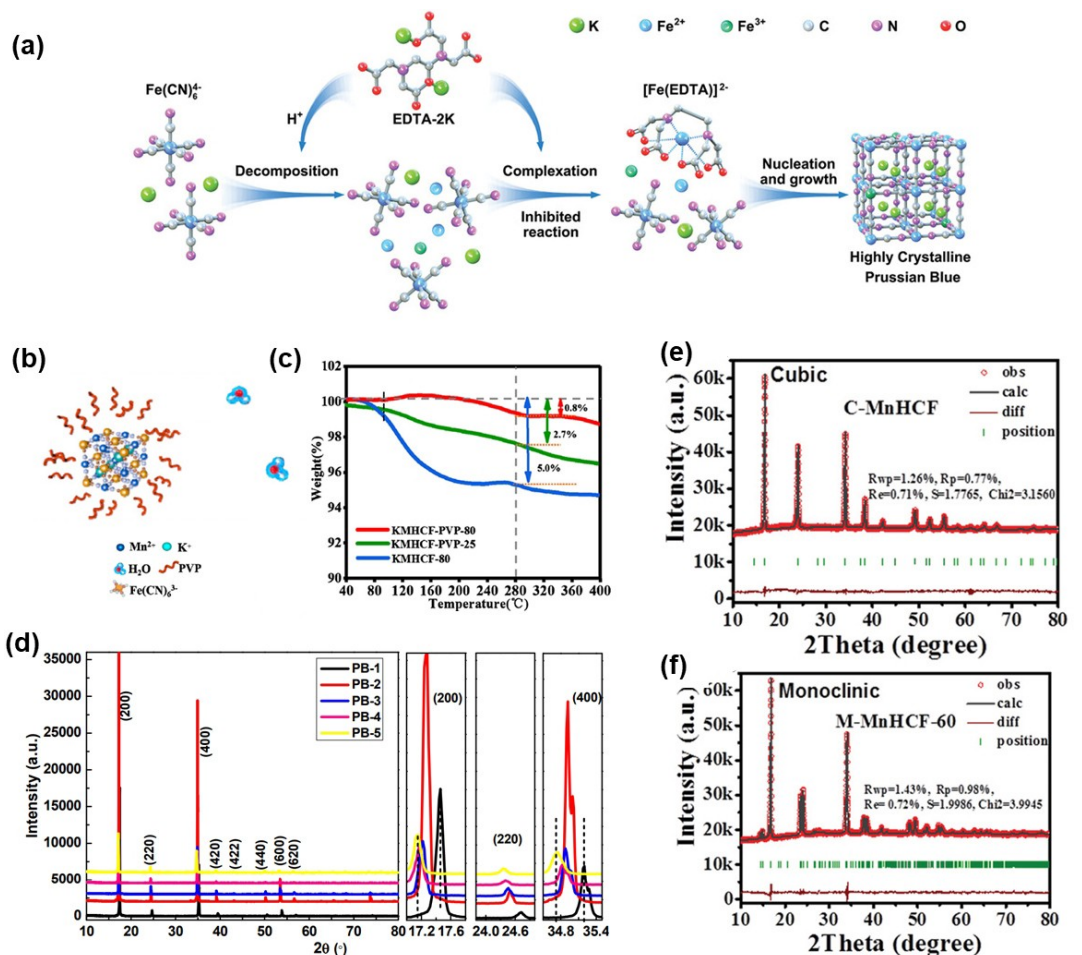


**Figure 8.** Schematic diagram of (a) coprecipitation synthesis of  $K_{1.61}Fe[Fe(CN)_6]_{0.88} \cdot 0.43H_2O$  with EDTA chelating agent. Reprinted with permission from [115]. Copyright 2023, Wiley-VCH Verlag GmbH & Co. KGaA, Weinheim. (b) PVP-assisted crystallization process of potassium manganese hexacyanoferrate (KMnHCF). (c) Thermogravimetric Analysis (TGA) curves of KMnHCF synthesized at various conditions: KMHCF-80 (80 °C), KMHCF-PVP-25 (25 °C with PVP), and KMHCF-PVP-80 (80 °C with PVP). Adapted with permission from [117]. Copyright 2021, American Chemical Society. (d) XRD patterns of NaFeHCF samples with varying NaCl content. Adapted from [118]. Copyright 2015, American Chemical Society. XRD patterns of (e) cubic phase C-MnHCF ( $Na_{1.38}Mn[Fe(CN)_6]_{0.92}\square_{0.08} \cdot 2.57H_2O$ , synthesized at 25 °C) and (f) monoclinic phase M-MnHCF ( $Na_{1.90}Mn[Fe(CN)_6]_{0.93}\square_{0.07} \cdot 2.34H_2O$ , synthesized at 60 °C). Reprinted with permission from [76]. Copyright 2020, Wiley-VCH Verlag GmbH & Co. KGaA, Weinheim.

water occupying the vacancy decreases, resulting in better lattice ordering and results in superior cycling stability.<sup>[118]</sup>

While the addition of excess salt in the precursor solution is beneficial, suppressing oxidation of low valence metal ions and the ferrocyanide ion  $[Fe^{II}(CN)_6]^{4-}$  is equally important to achieve low-vacancy and alkali metal-rich frameworks.<sup>[108]</sup> Several efforts were made such as flowing or bubbling inert  $N_2$  gas during synthesis, adding reductants, and even synthesizing the materials in dark conditions. Other synthesis conditions such as temperature and atmosphere can also regulate the crystal phase of PBAs. In an MnHCF framework, the structure obtained at 25 °C was face-centered cubic (space group  $Fm-3m$ ) (Figure 8e) while at 60 °C and 80 °C, the product obtained was monoclinic (space group  $P21/n$ ) (Figure 8f). The monoclinic MnHCF ( $Na_{1.90}Mn[Fe(CN)_6]_{0.93}\square_{0.07} \cdot 2.34H_2O$ ) showed a phase transition from monoclinic to cubic to tetragonal phase upon being employed as a cathode for SIBs, which resulted in lower cycling stability compared to the cubic MnHCF ( $Na_{1.38}Mn[Fe(CN)_6]_{0.92}\square_{0.08} \cdot 2.57H_2O$ ).<sup>[76]</sup>

### 3.2. Composition Modification

Tailoring cathode material composition is frequently employed in battery research to tune the output voltage, capacity, cyclability, rate capability, and cost. In PBAs, this approach may be done in 2 ways: (1) elemental substitution or cationic doping, which alters the overall bulk composition, and (2) concentration gradient which varies the composition along the depth of the framework.

#### 3.2.1. Bulk Elemental Substitution

Element doping is a versatile technique that exerts a direct influence on the structural integrity and redox behavior of the cathode material. Transition metal doping (Figure 9a) is carried out by combining salts of the desired transition metals (i.e.,  $FeCl_2$  and  $NiCl_2$  with a ferro/ferricyanide source), either by coprecipitation or hydrothermal method. The effect of doping

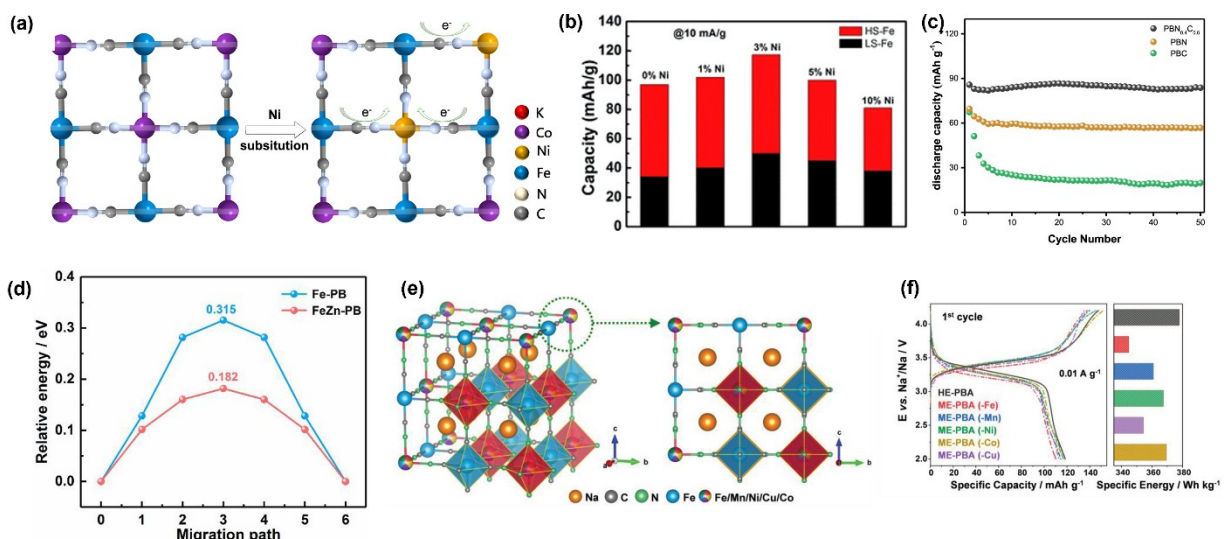


**Figure 9.** (a) Schematic illustration of Ni substitution in CoHCF. Adapted with permission from [121]. Copyright 2019, American Chemical Society. (b) Capacity contribution of HS-Fe and LS-Fe in FeHCF with increasing Ni content. Reproduced with permission from [120]. Copyright 2017, The Royal Society of Chemistry. (c) Cycling performance of Ni-doped CoHCF ( $K_{1.49}Ni_{0.36}Co_{0.64}[Fe(CN)_6]_{0.91}\cdot0.89H_2O$ ). Adapted with permission from [121]. Copyright 2019, American Chemical Society. (d) Energy barrier of the migration of  $Na^+$  ions in FeHCFs (Fe-PB) and Zn-doped FeHCFs (FeZn-PB). Adapted with permission from [123]. Copyright 2021, Elsevier. (e) Schematic diagram of multi-element substitution in an entropy-driven approach and (f) specific capacity and energy of high entropy PBAs and medium entropy PBAs. Reprinted with permission from [126]. Copyright 2021, The Authors. Advanced Materials published by Wiley-VCH GmbH.

on the electrochemical performance varies depending on the nature of the dopant and the metal to be substituted.

Partial substitution of Fe with Ni was found to not only improve its cycling stability and rate performance but also activate the C-coordinated  $Fe^{2+}/Fe^{3+}$  couple for efficient sodium-ion storage.<sup>[119,120]</sup> Fu et al. discovered that the capacity contribution of the C-connected Fe was higher for FeHCF doped with 3% Ni compared to the undoped framework (Figure 9b). However, it is important to note that while increasing the amount of Ni in the framework also increases its cycling stability, this leads to a decrease in discharge capacity due to a reduction in available redox sites.<sup>[120]</sup> In the case of CoHCFs, doping with Ni was also found to improve their cyclability (Figure 9c) by minimizing lattice strains during  $Na^+/K^+$  de-/intercalation in both SIBs ( $Na_{0.71}Ni_{0.25}Co_{0.75}[Fe(CN)_6]_{0.75}$ )<sup>[48]</sup> and KIBs ( $K_{1.49}Ni_{0.36}Co_{0.64}[Fe(CN)_6]_{0.91}\cdot0.89H_2O$ ),<sup>[121]</sup> respectively.

Aside from Ni, Zn and Cu dopants have been recently investigated to have stabilizing effects in PBA frameworks.<sup>[122–125]</sup> For example, Zn, a low-cost alternative to Ni, was employed to synthesize  $Na_{1.98}Fe_{0.89}Zn_{0.11}[Fe(CN)_6]_{0.90}\square_{0.10}\cdot1.60H_2O$  (Fe-ZnPb) with reduced adsorbed water and vacancies compared to the undoped  $Na_{1.93}Fe[Fe(CN)_6]_{0.86}\square_{0.14}\cdot1.63H_2O$  (Fe-PB), resulting in improved structural integrity and enhanced cycling stability.<sup>[122,123]</sup>

Furthermore, X-Ray Photoelectron Spectroscopy (XPS) analysis shows that the relative amount of  $Fe^{2+}$  vs  $Fe^{3+}$  is increased in Fe-ZnPb, indicating that Zn substitution also attenuates the unavoidable oxidation of  $Fe^{2+}$  and consequently increases the  $Na^+$  content in the structure. The decreased energy barrier and smaller bandgap observed in Fe-ZnPb (Figure 9d) suggest that Zn doping enhances  $Na^+$  ion migration ability and improves electronic conductivity, which contributes to the increased

capacity of Zn-doped FeHCFs.<sup>[123]</sup> Like Ni, Cu has also been observed to activate the C-connected Fe atom in  $Na_{1.68}Fe_{0.92}Cu_{0.08}[Fe(CN)_6]_{0.86}\square_{0.14}\cdot1.43H_2O$ , in addition to its structure-stabilizing effect resulting from its electrochemical inactivity within the working potential window (2.0–4.0 V). Moreover, Cu doping has demonstrated its capability to regulate the occurrence of side reactions at the electrode-electrolyte interface to a certain extent.<sup>[125]</sup> On the other hand, Ma et al. employed an entropy-driven stabilization approach in PBAs, where five transition metals were co-introduced at the N-coordinated lattice site in equimolar fractions to form the high-entropy PBA ( $(Na_{1.19}(Fe_{0.2}Mn_{0.2}Ni_{0.2}Cu_{0.2}Co_{0.2})[Fe(CN)_6]_{0.79}\square_{0.21}\cdot1.16H_2O$ ) (Figure 9e). Owing to the absence of phase transitions, this high entropy PBA exhibits a more robust structure, increased initial specific capacity (Figure 8f), and better cycling stability compared to conventional PBAs.<sup>[126]</sup>

### 3.2.2. Concentration Gradient

Concentration-gradient design, being a complex variation of bulk cationic doping, is a novel strategy in which the PBAs have varying elemental composition from the interior to the surface of the particle (Figure 10a).<sup>[127]</sup> Concentration-gradient PBAs are formed by changing the amounts of the transition metal ions that link the hexacyanometallate ions (i.e.,  $M_1$  and  $M_2$  in  $A_xM_1M_2[M'(CN)_6]_y\cdot zH_2O$ ) which can be synthesized via a coprecipitation process that starts with slowly adding a salt solution of  $M_1$  to the salt solution of  $M_2$ , thus increasing the  $M_1$  concentration in the latter solution with time (Figure 10b).<sup>[128]</sup> Simultaneously, the solution of combined  $M_1$  and  $M_2$  is mixed

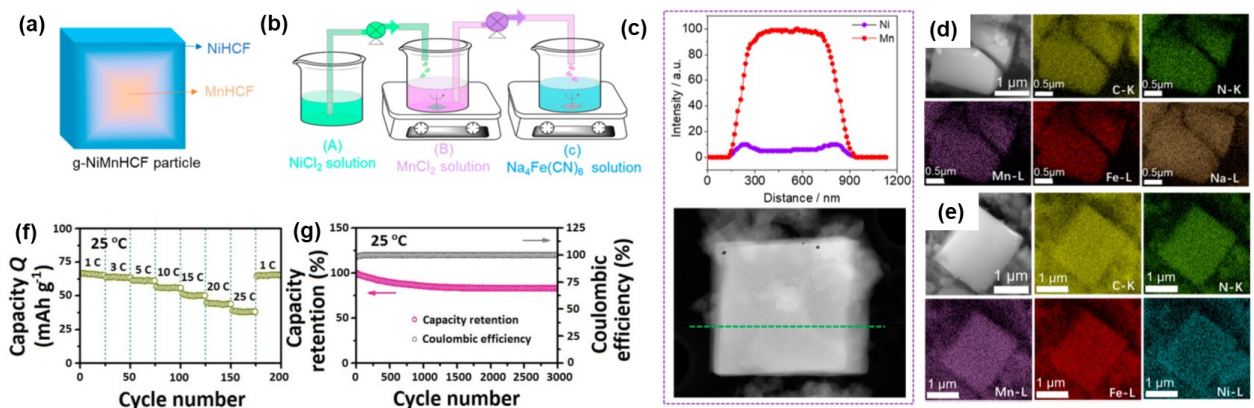


**Figure 10.** (a) Illustration of concentration-gradient particle. (b) Schematic diagram of synthesizing gradient particle. (c) STEM image and energy dispersive X-ray spectroscopy (EDS) linear scan of gradient- $(\text{Ni}_{0.3}\text{Mn}_{0.7})\text{HCF}$  ( $\text{Na}_{1.37}(\text{Ni}_{0.28}\text{Mn}_{0.72})[\text{Fe}(\text{CN})_6]_{0.84} \cdot 2.39\text{H}_2\text{O}$ ). SEM images and elemental mapping of (d) MnHCF and (e) gradient- $(\text{Ni}_{0.1}\text{Mn}_{0.9})\text{HCF}$  ( $\text{Na}_{1.17}(\text{Ni}_{0.12}\text{Mn}_{0.88})[\text{Fe}(\text{CN})_6]_{0.79} \cdot 1.5\text{H}_2\text{O}$ ) after 100 cycles. Adapted with permission from [128]. Copyright 2019, American Chemical Society. (f) Rate capabilities at different current densities, and (g) Long-term cycling of  $\text{K}_{1.84}[\text{Fe}_{0.31}\text{Mn}_{0.69}][\text{Fe}(\text{CN})_6]_{0.94} \cdot 1.25\text{H}_2\text{O}$ . Reprinted with permission from [80]. Copyright 2022, Science Press and Dalian Institute of Chemical Physics, Chinese Academy of Sciences. Published by ELSEVIER B.V. and Science Press.

with an aqueous solution containing  $\text{A}_3[\text{M}(\text{CN})_6]$  to form the gradient PBAs.

Concentration gradient can also exist by varying the amounts of hexacyanometallate ions (i.e., M' and M'' in  $\text{A}_x\text{M}[\text{M}'(\text{CN})_6]_y[\text{M}''(\text{CN})_6]_{1-y} \cdot z\text{H}_2\text{O}$ ) which can be synthesized via similar coprecipitation method as previously mentioned but having separate solutions of  $\text{A}_3[\text{M}'(\text{CN})_6]$  and  $\text{A}_3[\text{M}''(\text{CN})_6]$  instead of the M<sub>1</sub> and M<sub>2</sub> salts solutions.<sup>[127]</sup> While nickel has been widely reported as a promising metal dopant in DE-PBAs with zero-strain property as it improved structural integrity, and thus, cycling stability, the incorporation of electrochemically inactive nickel drastically reduces the material's discharge capacity. Using concentration-gradient PBAs with Ni-rich surface is the solution to minimizing the detrimental consequences of having Ni all throughout the bulk because nickel is advantageously introduced only in select particle regions. Hu et al. presented concentration-gradient  $\text{Na}_x\text{Ni}_y\text{Mn}_{1-y}\text{Fe}(\text{CN})_6 \cdot n\text{H}_2\text{O}$  with increasing Ni concentration and decreasing Mn concentration from the center (Figure 10c).<sup>[128]</sup> The mechanical stability of the NiHCF-rich surface, and thus of the whole concentration-gradient particle, as displayed by the lack of obvious fractures from Scanning Electron Microscopy (SEM) images after 100 cycles (Figure 10d–e), resulted in the improved capacity retention of 95%, compared to MnHCF's retention of 52.5% after 100 cycles.

Aside from nickel's beneficial addition to MnHCFs, Wang et al. demonstrated that nickel gradient also served two purposes in FeHCF (i.e.,  $\text{Na}_{1.04}\text{Fe}_{0.83}\text{Ni}_{0.17}[\text{Fe}(\text{CN})_6]_{0.76} \cdot 2.36\text{H}_2\text{O}$ ).<sup>[129]</sup> The high-Ni-content outer layer controlled the side reactions with the electrolyte by limiting the available Fe that contacted the organic electrolyte, as confirmed by the absence of a weak cathodic peak during CV and by the maintained cubic morphology without obvious structure collapse from SEM images of the high Ni gradient PB.

Meanwhile, Lin et al. designed a binary hexacyanoferrate (i.e.,  $\text{K}_x\text{Fe}_y\text{Mn}_{1-y}[\text{Fe}(\text{CN})_6] \cdot n\text{H}_2\text{O}$ ) nanocuboid with decreasing Mn content from the center to the surface.<sup>[80]</sup> The high structural

integrity of the gradient architecture realized high energy density (41 Wh kg<sup>-1</sup> at a power density of 1.8 kW kg<sup>-1</sup>) and high capacity retention (83% during 3,000 cycles at 5 C) (Figure 10f–g). These examples demonstrated that concentration-gradient design is a worthwhile modification strategy for exploring PBAs as cathode materials.

### 3.3. Morphology and Particle Size Control

Modification of PBA's morphology, via tuning of synthetic conditions, is another promising approach to improving their performance with hollow structures having closed single-shelled, open, or hierarchical designs showing the greatest improvements (Figure 11a).<sup>[130]</sup>

Closed single-shelled hollow structures are the most common structures that can be synthesized either through a soft templating approach in which the shell material deposit between emulsion droplets or through a hard templating approach in which the templating agent also participates as reactant in the process.<sup>[131]</sup> Open hollow structures, referred to as polyhedral cages or frames, are polyhedron shells with partial or complete openings on their walls, while hierarchical hollow structures have complex boundaries and cavities with tailored physicochemical properties.<sup>[131]</sup> PBAs with unique morphologies exhibited enhanced diffusion kinetics, as observed in hollow structures showing advantages in electrochemical performance compared to solid structures.<sup>[130]</sup> Luo et al. revealed the mechanism of synthesizing Co- and Fe-containing hollow structures from solid structures through a hard templating method (Figure 11b–d).<sup>[132]</sup> The hollow structure displayed fewer water-induced structural defects and shorter electron/ion diffusion pathways when used as a cathode for SIBs which translated to an improved capacity of 95.7 mAh g<sup>-1</sup> compared to 60 mAh g<sup>-1</sup> of the traditional PBA after 100 cycles. Complex structures such as hierarchical hollow rod-like PB have also been synthesized and applied as cathode materials in SIBs by

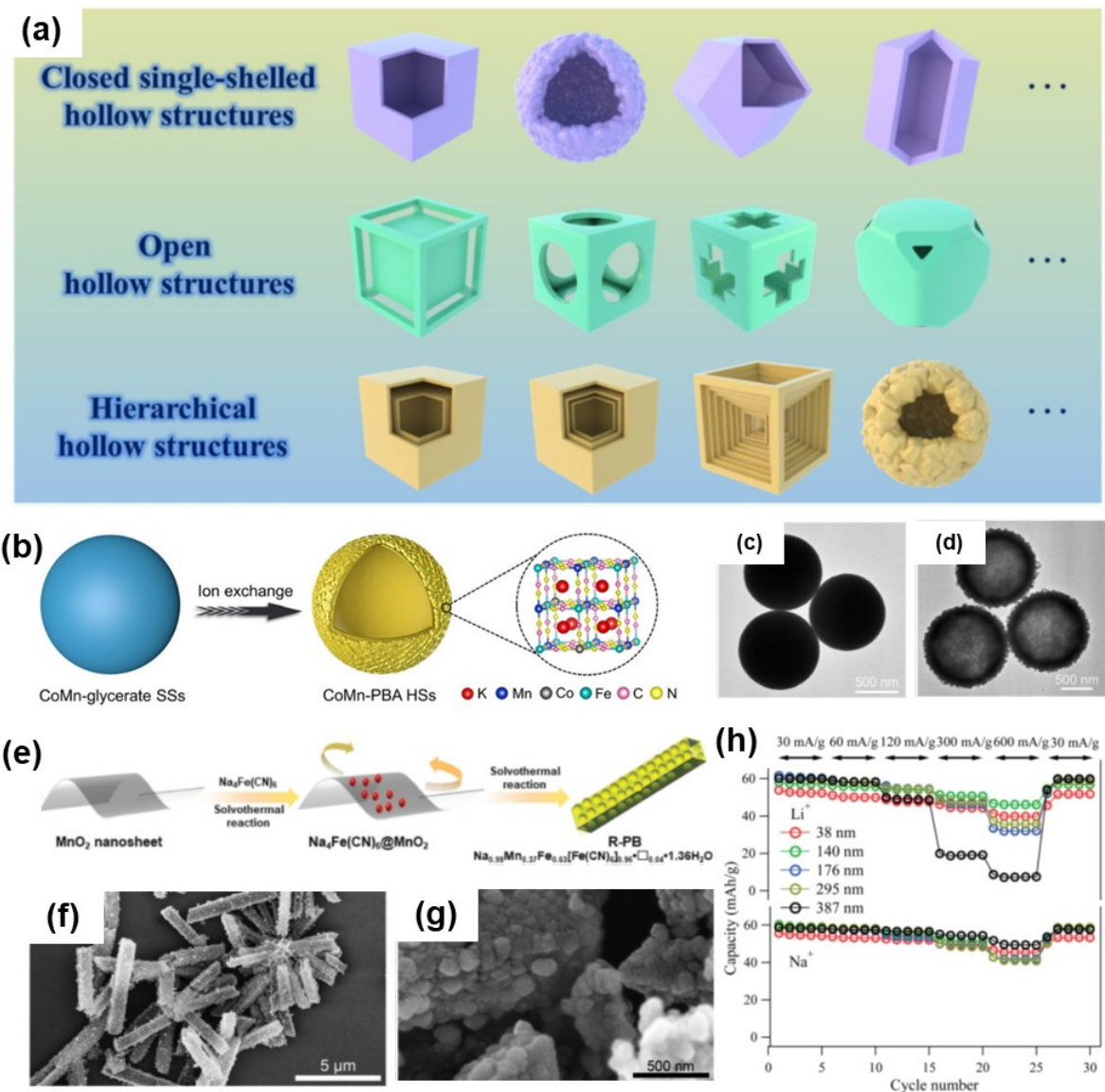


**Figure 11.** (a) Schematic drawing of different hollow structures. Adapted with permission from [138]. Copyright 2023, The Authors. Carbon Neutralization published by Wenzhou University and John Wiley & Sons Australia, Ltd. (b) Synthesis of hollow-structured PBA from solid-structured particle. Transmission Electron Microscopy (TEM) images of (c) solid-structured CoMn-glycerate and (d) hollow-structured  $K_{1.34}Co_{0.23}Mn_{0.88}[Fe(CN)_6]$ . Reprinted with permission from [135]. Copyright 2021, The Authors. Angewandte Chemie International Edition published by Wiley-VCH Verlag GmbH & Co. KGaA, Weinheim. (e) Synthesis of hierarchical rod-like PB. (f–g) SEM images of rod-like PBA. Reprinted with permission from [133]. Copyright 2018, Wiley-VCH Verlag GmbH & Co. KGaA, Weinheim. (h) Rate capability of  $KNi[Fe(CN)_6]$  with different particle sizes. Adapted with permission from [137]. Copyright 2014, The Royal Society of Chemistry.

Feng et al. (Figure 11e–g).<sup>[133]</sup> The low number of vacancies and coordinated water of the hollow PB limited the volume change during the charge-discharge process, while the activation of iron's redox transition at high voltage from Mn substitution realized a discharge capacity of  $117.3 \text{ mAh g}^{-1}$  at 1 C and a capacity retention of 98.5 % after 200 cycles.

Aside from SIBs, PBAs with hollow structures had been explored in ZIBs with Zeng et al. reported the construction of Co-substituted Mn-rich PBA hollow spheres ( $K_{1.34}Co_{0.23}Mn_{0.88}[Fe(CN)_6]$ ) and Cu-substituted MnHCF double-shelled nanoboxes.<sup>[134,135]</sup> Aside from suppressing Jahn-Teller distortion from Co and Cu substitution, the structural advantage of the hollow structure ensured a large surface area and provided rich

active sites with fast  $Zn^{2+}$  ion diffusion.<sup>[135]</sup> The Co-substituted hollow sphere with thin shell, compared to control samples of nanocubes and thick-shelled hollow spheres with similar transition metals (Co and Mn), displayed high reversible capacity ( $128.6 \text{ mAh g}^{-1}$  at  $0.05 \text{ A g}^{-1}$ ) and high rate capability ( $50.4 \text{ mAh g}^{-1}$  at  $2 \text{ A g}^{-1}$ ), while the Cu-substituted MnHCF double-shelled nanoboxes displayed impressive cycling stability (96.8 % retention after 2,000 cycles).<sup>[134,135]</sup>

Particle size engineering has shown that small particle size displayed superior performance, but also showed different effects when combined with other modification approaches.  $Na_{0.9}Fe[Fe(CN)_6]_{0.96}$  with ultrafine particles of 40 nm synthesized through a dry-milling method exhibited good capacity

(106 mAh g<sup>-1</sup>) and retention (80%) after 500 cycles at 10 C in SIBs.<sup>[136]</sup> In a different study, Li et al. reported that the reduction of particle size from 400 nm to 40 nm of K<sub>0.5</sub>Ni[Fe(CN)<sub>6</sub>]<sub>0.825</sub>·6.5H<sub>2</sub>O improved the rate capability of Li-ion intercalation while showing insignificant change for Na-ion intercalation (Figure 11h).<sup>[137]</sup> For K-ion intercalation in K<sub>1.94</sub>Mn[Fe(CN)<sub>6</sub>]<sub>1.0</sub>, Hosaka et al. concluded that small particle sizes (around 200 nm) resulted in large initial capacity and good rate performance, but the introduction of anion vacancies removed any advantages of size control.<sup>[138]</sup> Here, the synergistic effect of particle size with other modifications offers a new direction to improve PBA performance.

### 3.4. Surface Engineering

Coating or mixing with conductive polymers has also attracted attention to increase the electrical conductivity, and thus the electrochemical performance of PBAs as cathode materials.

Huang et al. coated hollow-structured Na<sub>1.65</sub>Co[Fe(CN)<sub>6</sub>]<sub>0.88</sub>□<sub>0.12</sub>·1.1H<sub>2</sub>O with polydopamine to improve stability and suppress any structural strain during Na intercalation (Figure 12a–c).<sup>[140]</sup>

Compared with the uncoated hollow-structured PBA, the polydopamine-coated material exhibited a 14.3% higher capacity retention after 100 cycles and reached 88 mAh g<sup>-1</sup> at 0.1 A g<sup>-1</sup> after 500 cycles with its high reversibility being attributed to the stable phase structure during cycling. Similar improvements were seen in polypyrrole-coated K-rich FeHCF (K<sub>1.87</sub>Fe[Fe(CN)<sub>6</sub>]<sub>0.97</sub>□<sub>0.03</sub>·0.84H<sub>2</sub>O) as cathode material for KIBs.<sup>[85]</sup> In addition to increasing the electronic conductivity, the polypyrrole-coated sample had lower lattice defect concentration, thus showed a high capacity retention (86.8% after 500 cycles at 50 mA g<sup>-1</sup>) and rate capability (61.8 mAh g<sup>-1</sup> after 500 cycles at 1000 mA g<sup>-1</sup>). With polypyrrole having a high electronic conductivity (102 S cm<sup>-1</sup>) among polymers, it had also been considered a promising additive in aqueous hybrid batteries with Ruan et al. investigating the effect of polypyrrole-

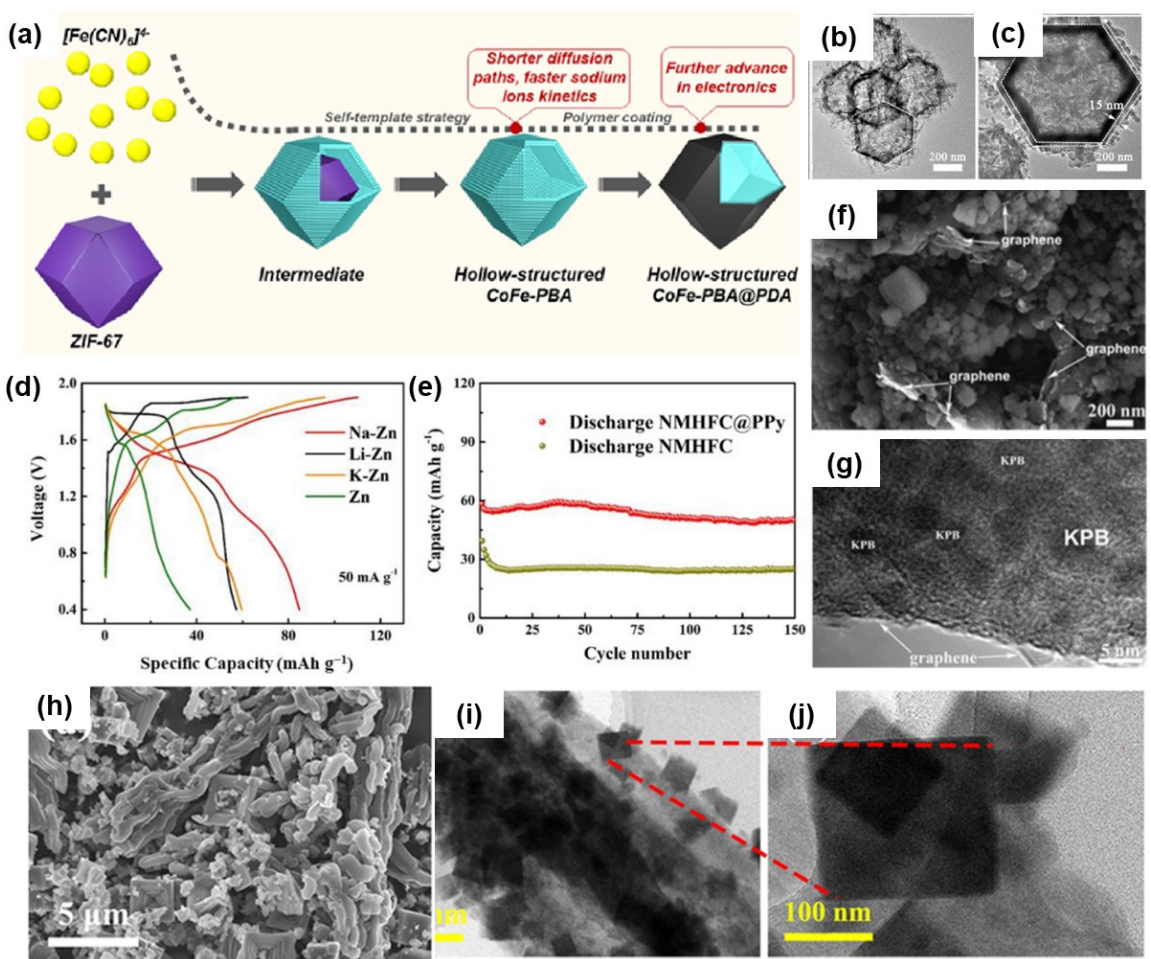


**Figure 12.** (a) Synthesis of polydopamine-coated PBA. TEM images of (b) hollow-structured PBA and (c) polydopamine-coated PBA with hollow structure. Adapted from [140]. Copyright 2021, American Chemical Society. (d) Voltage profiles of Na<sub>2</sub>MnFe(CN)<sub>6</sub>@PPy in different hybrid electrolytes. (e) Cycling performance at 200 mA g<sup>-1</sup> of Na<sub>2</sub>MnFe(CN)<sub>6</sub>@PPy. Adapted from [141]. Copyright 2022 by the authors. Licensee MDPI, Basel, Switzerland. (f) SEM image, and (g) High-Resolution Transmission Electron Microscopy (HRTEM) image of K<sub>1.85</sub>Mn[Fe(CN)<sub>6</sub>]<sub>0.96</sub>□<sub>0.02</sub>·0.7H<sub>2</sub>O with graphene. Reproduced with permission from [82]. Copyright 2019, The Royal Society of Chemistry and the Centre National de la Recherche Scientifique. (h) SEM image of hollow PB cubes with mesoporous carbon. (i-j) TEM image of hollow PB cubes with mesoporous carbon. Adapted with permission from [142]. Copyright 2021, American Chemical Society.

coated MnHCF ( $\text{Na}_2\text{MnFe}(\text{CN})_6@\text{PPy}$ ) in hybrid Li–Zn, Na–Zn, and K–Zn batteries with the Na–Zn combination having the best electrochemical performance (Figure 12d–e).<sup>[141]</sup> Without affecting the morphology and size of the original PBA, this coating strategy resulted in a discharge capacity of  $55.0 \text{ mAh g}^{-1}$  (vs  $25.2 \text{ mAh g}^{-1}$  of the uncoated PBA) after 10 cycles in the aqueous Na–Zn hybrid electrolyte.

Interestingly, nanocomposites have been shown to increase the electrical conductivity of PBAs. Ball milling of  $\text{K}_x\text{MnFe}(\text{CN})_6$  with graphene resulted in small grains (40–80 nm) that were attached to the surface of graphene (Figure 12f–g).<sup>[82]</sup> The PBA with graphene ( $\text{K}_{1.85}\text{Mn}[\text{Fe}(\text{CN})_6]_{0.98}\square_{0.02}0.7\text{H}_2\text{O}$ ) delivered a discharge capacity of  $100.2 \text{ mAh g}^{-1}$  (vs  $39.6 \text{ mAh g}^{-1}$  for the bare PBA) at a high discharge rate of 10 C. Furthermore, Wang et al. reported a continuous conductive network of hollow PB cubes on mesoporous carbon to solve the electrical conductivity issue and to increase surface area (Figure 12h–j).<sup>[142]</sup> The rapid electron/ion migration due to the low resistance and high capacitive distribution ratios resulted in low half-cell polarization and in a discharge capacity of 120 and  $87 \text{ mAh g}^{-1}$  at current densities of 100 and  $3200 \text{ mA g}^{-1}$ , respectively.

## 4. Critical Parameters for Commercialization

While LIBs are positioned as the leading commercial energy storage solution due to their performance and technological maturity, the availability of critical raw materials such as lithium and cobalt limits their future growth. Extensive efforts have been carried out to deem PLBs for commercial viability, however, most of these chemistries (especially MVIBs) necessitate further research and are therefore not yet commercialized.

On the other hand, SIBs are rapidly catching up in the evolving energy storage landscape, owing to their compatibility with existing manufacturing techniques that have already been optimized for LIBs (Figure 1a). Companies such as Novasis Energies Inc., Faradion Limited,<sup>[17]</sup> HiNa Battery Technology, Contemporary Ampere Technology Co., Limited (CATL),<sup>[62]</sup> ALTRIS,<sup>[143]</sup> TIAMAT,<sup>[144]</sup> and Natron Energy<sup>[75]</sup> are among the major players that have focused their research on commercializing SIBs. Specifically, Natron Energy, Novasis, CATL, and ALTRIS employ PBA full-cell chemistries owing to their facile synthesis, environmental benignity, and well-balanced combination of specific capacity and framework stability, when compared to its layered oxide counterparts. In 2022, a battery startup Group1 seeks to be the world-first in commercializing KIBs and will employ a novel potassium-PW cathode material, which promises long cycle life, high efficiency, and fast-charging ability.<sup>[145]</sup> To further advance PLBs for future development, this section delves into the critical aspects that should be considered to endow PBAs for future practical applications.

### 4.1. Performance

The evaluation of battery electrochemical performance is centered on three key parameters: energy density, electromotive force, and cycle life (Table 2), which are heavily dependent on cathode materials.

While PBAs have a moderately high theoretical capacity ( $170 \text{ mAh g}^{-1}$ ), this is often underachieved due to the presence of defects such as vacancies and crystal water. In 2021, CATL was able to achieve a full-cell energy density of  $160 \text{ Wh kg}^{-1}$  by utilizing a Na-rich PW cathode material.<sup>[75]</sup> On the other hand, Novasis Energies Inc., in collaboration with the University of Texas, employed  $\text{Na}_x\text{MnFe}(\text{CN})_6$  ( $x=0\text{--}2$ ) as a cathode and sodium metal as an anode in a coin cell and started with a specific capacity of  $68 \text{ mAh g}^{-1}$ . Reversible capacity was increased to  $134 \text{ mAh g}^{-1}$  as a result of improvements such as increased  $\text{Na}^+$  content in the precursor solution during coprecipitation.<sup>[17,146]</sup> After employing further synthesis modifications, the attained energy density is  $\sim 542 \text{ Wh kg}^{-1}$  which aligns comparably with that of commercial  $\text{LiFePO}_4$  (LFP) commonly used in LIBs.<sup>[17]</sup>

Thus, various optimization strategies, such as those mentioned in the preceding section, as well as a systematic understanding of the crystallization process of PBA crystals in the framework (i.e., precise control of vacancies and coordinated water), are crucial for improving electrochemical performance and for laying the groundwork for the commercialization of PLBs.

### 4.2. Cathode Material Scale-Up Production

Scalable preparation of active materials is necessary to achieve the practical application of PBA-based batteries. Generally, laboratory-scale synthesis of PBAs is carried out in a beaker, obtaining homogeneous aqueous solutions through the coprecipitation method, with around 1 g yield per batch.<sup>[17]</sup> Several efforts have been made to scale up the preparation of PBAs. For instance, Liaoning Starry Sky Sodium-ion Battery Co., Ltd. (China), in collaboration with the University of Wollongong, scaled up the synthesis of PBAs using a coprecipitation method in a 100 L (Figure 13a–c) and a 500 L reactor based on a 1 L beaker-scale coprecipitation, with no compromise in its electrochemical performance and quality.<sup>[143]</sup> In 2018, Novasis was able to successfully scale up the quantity of PBAs to 10 kg/batch, and up to 100 kg per batch (Figure 13d) while still maintaining the intended electrochemical performance.

Recently, a scaled-up preparation of a binary Mn/Ni-PB was prepared by Xu et al., using a 100 L reactor, yielding 3.3 kg per batch (Figure 13e), with the same monoclinic phase and good crystallinity as the beaker-synthesized PBA.<sup>[147]</sup> Despite the simple preparation of PBAs, it is critical to determine the scale-up process parameters (i.e., temperature, pressure, mixing time) to have as much congruence with the small batch as possible while not compromising the quality and crystal properties, as well as the consistency between batches. Additionally, the low yield of PBAs from coprecipitation, particularly when nano-

**Table 2.** Parameter comparison between representative PBA-based PLBs and other commercial battery technologies.

	Energy Density (Wh kg <sup>-1</sup> )	Average Voltage (V)	Cycle life (Cycle Number)	Key Characteristics	Intended Applications	Ref.
SIB (PBA cathodes: Na <sub>2-x</sub> Fe[Fe(CN) <sub>6</sub> ])	25–160	~3.1	up to 6000	Long cycle life, wide temperature range	Grid energy storage (not limited by mass or volume)	[16–19, 148, 149]
SIB (Layered oxide cathodes: Na <sub>a</sub> Ni <sub>(1+x+y-z)</sub> Mn <sub>x</sub> Mg <sub>y</sub> Ti <sub>z</sub> O <sub>2</sub> )	120–170	~3.0	up to 5000	High energy, low cost	Two-wheeler to four-wheeler vehicles (short to medium range)	[17, 20, 148, 150]
SIB (Polyanionic compound cathodes: Na <sub>3</sub> V <sub>2</sub> (PO <sub>4</sub> ) <sub>2</sub> F <sub>3</sub> , Na <sub>3</sub> VC(PO <sub>3</sub> ) <sub>3</sub> , Na <sub>4</sub> Fe <sub>3</sub> (PO <sub>4</sub> ) <sub>2</sub> (P <sub>2</sub> O <sub>7</sub> ))	90–160	~3.4	up to 6000	High power, fast charge	Power tools	[21, 148, 150]
LIB (LiFePO <sub>4</sub> /graphite)	90–130	3.2–3.3	1000–2000	High safety, long cycle life	Electric vehicles with lower performance requirements	[151, 152]
LIB (LiNi <sub>1-x,y</sub> Co <sub>x</sub> Al <sub>y</sub> O <sub>2</sub> /Graphite)	200–260	3.6–3.65	500	Thermally stable, low cost	EV (large format batteries)	[152, 153]
LIB (LiNi <sub>1-x,y</sub> Mn <sub>x</sub> Co <sub>y</sub> O <sub>2</sub> /Graphite)	150–220	3.8–4.0	1000–2000	Thermally stable, low cost	Portable consumer electronics, Plug-in Hybrid Electric Vehicles (PHEV)	[152, 153]
LIB (LiMn <sub>2</sub> O <sub>4</sub> /Graphite)	100–150	3.7–4.0	300–700	High power	Automotive industry (starting, lighting, and ignition batteries)	[152, 153]
Lead-acid battery	25–40	2.1	1000	Low-cost, maintenance-free	Automotive industry (starting, lighting, and ignition batteries), stationary (load levelling, averaging demand peaks)	[151, 154]
Vanadium redox flow battery	10–20	1.4	5000	Long cycle life, high mechanical stability	Stationary applications (utility-scale, microgrids, off-grid)	[21, 151]
Nickel metal hydride battery	40–110	1.2	600–1000	High power, constant-voltage discharge	High-current-drain applications (digital cameras)	[155, 156]
Sodium-sulfur battery	150–240	2.1	3500–5000	High energy efficiency, long cycle life	Grid applications (emergency power, electric transmission, and distribution system support)	[21, 151, 157, 158]

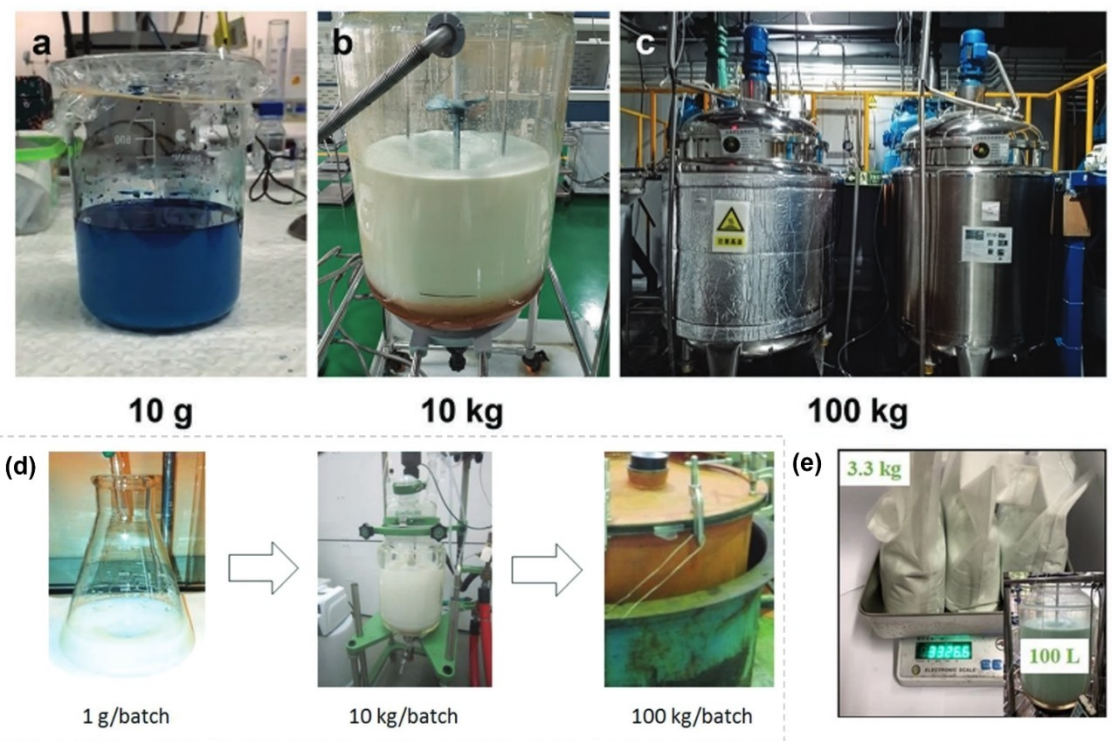


**Figure 13.** Scale-up synthesis of PBAs with (a) 10 g yield, (b) 10 kg yield, and (c) 100 kg yield. Reprinted from [143]. Copyright 2022 by Wiley-VCH GmbH. (d) Synthesis of PW from 1 g/batch to 100 kg/batch yield. Adapted with permission from [17]. Copyright 2018, Wiley-VCH Verlag GmbH & Co. KGaA, Weinheim. (e) 3.3 kg yield from 100 L reactor. Adapted with permission from [147]. Copyright 2022, American Chemical Society.

particles are prepared, remains a challenge that needs to be addressed. In terms of raw material availability, PBA precursors such as transition metal salts are abundant and readily accessible, making PBAs advantageous for scaling up.

#### 4.3. Mass Fabrication of Full Cells

The ease and compatibility of fabricating full cells with the currently developed LIB processing facilities will aid in the commercialization of PLBs. The rational design of PBA-based full cells, including its components (i.e., anode, electrolyte, current collector), is linked to the cell's specific chemistry and intended application. While PBAs have been proven beneficial to aqueous battery chemistries, recent efforts for commercialization are focused on cells with organic electrolytes due to their wider working potential range, which will be more competitive with LIBs. SIBs and KIBs have the same fabrication method as LIBs, including slurry preparation (active material, conductive agent, solvent), electrode coating and drying, calendering, electrode and separator slitting, stacking and winding, electrolyte filling, and sealing (Figure 14a).<sup>[159]</sup>

However, to date, only SIB full cells have been tested for large-scale battery fabrication. To demonstrate, Novasis' pilot-line-scale electrode and pouch cell fabrication process (Figure 14b) employs a comma coater to obtain homogeneous coatings with favorable adhesion to Al current

collectors.<sup>[17]</sup> Liaoning Starry Sky Sodium-ion Battery Co., Ltd. demonstrated another pilot-line-scale fabrication process (Figure 14c), and they successfully mass-produced 5 Ah Fe-PBA || Hard carbon cells (Figure 14d) with Na-rich cathode, exhibiting a long cycling stability with ~78% capacity retention for over 1000 cycles (1.0–3.2 V) at 1 C rate.<sup>[49,143]</sup>

Larger PBA-based SIB productions were carried out by Natron Energy, through a collaboration with Lonza Specialty Ingredients (Basel, Switzerland), using the existing Li-ion production standard infrastructure, with a targeted annual battery production capacity of 600 MW beginning in 2022.<sup>[16]</sup> Additionally, they have also partnered with ABB Power Conversion to develop battery modules comprising 32 cells derived from individual 4.6 Ah pouch cells, with an overall voltage range of 32 V–58 V and a gravimetric energy density of  $10.3 \text{ Wh kg}^{-1}$ , which is intended for backup power applications.

Despite previous efforts, PBA-based PLBs still fall short in large-scale production processes. More research is needed to be employed to bridge the gap between lab-scale cell fabrication and commercial fabrication, such as: (1) selecting optimal powder properties (i.e., particle size, specific surface area, conductivity) of active material, binder, and conductive agent; (2) obtaining good rheological properties of slurry which can be affected by mixing sequence and mixing process parameters;<sup>[160]</sup> (3) choosing the slurry coating method (i.e. spray coating, dip coating, comma bar coating);

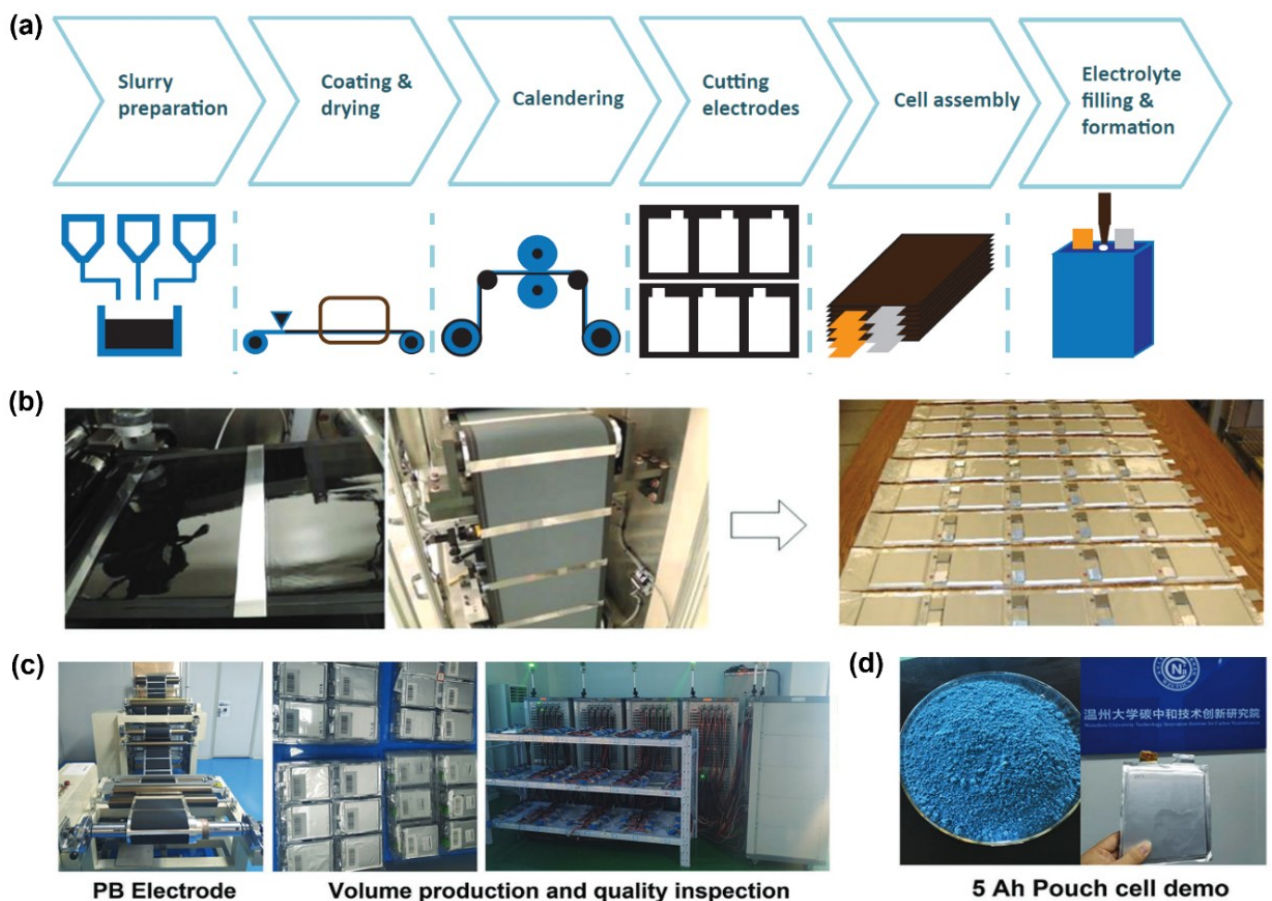


**Figure 14.** (a) Illustration of battery fabrication process. Adapted with permission from [161]. Copyright 2016, by the authors; licensee MDPI, Basel, Switzerland. (b) Photos of actual pilot line scale electrode preparation and pouch cell fabrication of Novasis Energies Inc. Reprinted from [17]. Copyright 2018, Wiley-VCH Verlag GmbH & Co. KGaA, Weinheim. Photos of Liaoning Starry Sky Sodium-ion Battery Co., Ltd.'s (c) Volume production of electrode and quality inspection. Reprinted from [143]. Copyright 2022 by Wiley-VCH GmbH. (d) 5 Ah pouch cell demo product. Adapted with permission from [49]. Copyright 2020, Springer Nature.

(4) optimizing electrode drying parameters; and (5) obtaining the desired thickness, porosity, density, and surface area of electrode through calendering.<sup>[159]</sup>

#### 4.4. Safety, Environmental Impact, and Cost

Safety, environmental impact, and cost are critical considerations when adopting new technology for commercial applications. It has been known that PBAs may emit toxic cyanide salts especially when subjected to higher temperatures, generally observed in hydrothermal decomposition of ferrocyanide precursor in acid.<sup>[162]</sup> Therefore, the coprecipitation method is preferred for better safety and less environmental impact. PBAs are generally thermally stable until  $\sim 300\text{ }^{\circ}\text{C}$ ,<sup>[163]</sup> to which above it, C≡N bonds start to be liberated.<sup>[143]</sup> The crystal water in the PBA framework also poses a serious safety issue especially when it reacts with the electrolyte and may lead to swelling due to gas release ( $\text{H}_2\text{O}$ ,  $\text{NH}_3$ ,  $\text{N}_2$ , HCN in the range of 25–350  $^{\circ}\text{C}$ ).<sup>[164]</sup>

Practical safety tests and quality control procedures such as decomposition tests at high temperatures, mechanical nail

penetration tests, and intentional overcharging can also be employed to determine harmful gas generation, temperature increase, possible ignition, short-circuiting, and swelling for a pouch cell.<sup>[17]</sup> For battery modules, a Battery Management System (BMS) must be present,<sup>[16]</sup> such as battery thermal management (BTM) with thermal sensors<sup>[152]</sup> to effectively monitor the temperature and mitigate possible risk of ignition due to overheating. Various advanced characterization techniques are highly recommended to gain a deeper understanding of gases generated, such as simultaneous online thermogravimetry mass spectrometry (TG-MS) and thermal analyzer.<sup>[164]</sup> Due to the intrinsic threat of water to the cell's safety, *in-situ* FTIR may be employed to investigate the mechanism and effects of crystal water during battery operation.<sup>[71]</sup>

The raw materials involved as well as the type of waste generated during the entire manufacturing process determine the environmental impact of a certain process. PBAs are considered to be environmentally friendly in terms of carbon emissions during mass production because coprecipitation does not require a high-temperature treatment. The aqueous solution involved, however, contains excess salts and additives such as surfactants and chelating agents, that remain when the

precipitate is washed through centrifugation or filtration. Finding ways on how to treat this solution before entering the effluent, or better yet, treating it so that it may be recycled and reused as an input to another process, could be a strategy to mitigate pollution.<sup>[165]</sup>

PBAs have low-cost and earth-abundant precursors as well as facile coprecipitation production process which makes them advantageous for lowering raw material cost and energy consumption. However, increased costs from modification strategies, additives, additional heat treatment, and dehydration steps, and post-treatment processes (i.e., wastewater treatment, and recycling techniques) must be taken into account.<sup>[165]</sup>

## 5. Conclusion and Perspective

The criticality of lithium necessitated the R&D of PLBs. This consequently propelled extensive materials research to develop components of these batteries, especially cathode.

This review provided an extensive overview of PBAs as cathode materials for PLBs, with a particular focus on their structure, mechanism, and electrochemical performance, as well as the remaining challenges that need to be addressed. While other metal ions ( $K^+$ ,  $Mg^{2+}$ ,  $Ca^{2+}$ ,  $Zn^{2+}$ , and  $Al^{3+}$ ) have shown great potential in aqueous and organic rechargeable batteries, most of them – especially higher valent ions – are still in the early stages of research, and the underlying mechanisms are still poorly understood.

Several challenges are yet to be addressed in employing PBAs as cathode materials for PLBs, such as vacancies, crystal water, side reactions, and conductivity issues. Nevertheless, different cathode modification strategies, such as crystallinity control, morphology engineering, and surface engineering, are being explored to mitigate these.

In order to accelerate the development of PBA-based PLBs, the following summarizes the key aspects that need profound research attention (Figure 15).

### 5.1. Electrolyte Modification

In addition to cathode modification, developing a compatible electrolyte system for PBAs is also crucial. Optimization of solvent, salt, additive, and concentration is necessary as these affect the energy density, CE, and the electrode-electrolyte interface component.<sup>[166]</sup> Organic electrolytes are the most commonly used, particularly ester- and ether-based solvents containing metal salts due to their high ionic conductivity combined with good wettability to separators and electrodes.<sup>[143,167]</sup> However, the use of organic liquid electrolytes often results to safety issues and side reactions with the cathode. Particularly, the increased susceptibility to side reactions in SIBs and KIBs compared to LIBs is due to the higher chemical reactivity of sodium and potassium, which leads to more intense reactions with traditional organic liquid electrolytes.<sup>[168]</sup> As a result, the search for an effective and safer

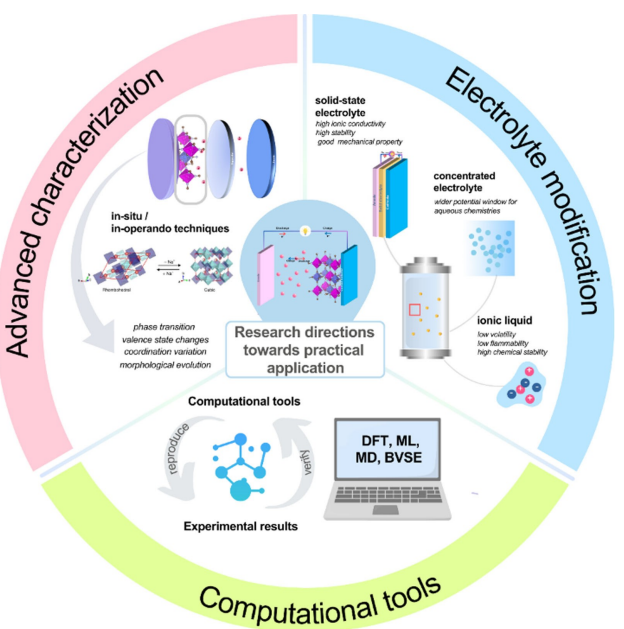


**Figure 15.** Research directions towards practical application of PBA-based PLBs. Phase transition in advanced characterization panel: Adapted with permission from [49]. Copyright 2020, Springer Nature.

electrolyte continues to be a major hurdle to the widespread use of PLBs.

Recently, water-in-salt (WIS) electrolytes for aqueous batteries,<sup>[169]</sup> ionic liquid,<sup>[170]</sup> and highly concentrated electrolytes<sup>[171]</sup> are being explored to stabilize the interface, enable wide voltage operation, and optimize the performance of PBA-based PLBs. In aqueous-based AlIBs, employing a highly concentrated 5 m  $Al(CF_3SO_3)_3$  WIS electrolyte enabled a wide potential window (~ 2.65 V), as well as good resistance to cathode dissolution, resulting in a high initial discharge capacity and long cycle life (> 100 cycles with 0.39% capacity fading per cycle).<sup>[172]</sup> The use of ionic liquids is also promising because of their low volatility/flammability, high chemical and electrochemical stability, and inherent ionic conductivity.<sup>[173]</sup> The use of an ionic liquid as electrolyte ((KFSI) in *N*-butyl-*N*-methylpyrrolidinium bis(fluorosulfonyl)imide (Pyr<sub>1,3</sub>FSI)) in KIB full cells with  $K_2Mn[Fe(CN)_6]$  cathode was found to be a viable method not only for minimizing irreversible capacity loss but also for suppressing the corrosion of Al current collector, resulting in high capacity retention (99% after 400 cycles).<sup>[174]</sup>

Another emerging trend is replacing these with solid-state electrolytes, which eliminate flammability issues and have excellent mechanical properties that can enable the practical application of PLBs under extreme temperature and pressure conditions.<sup>[143,175]</sup> For example, employing a solid-state polymer electrolyte for SIBs resulted in high rate capability (87.5 mAh g<sup>-1</sup> at 8 C) and long cycle life (1100 cycles at 1 C) with negligible capacity decay (~0.014% per cycle). The developed solid-state polymer membrane also demonstrated outstanding mechanical flexibility before and after freezing at -35 °C, which is a good way of preventing short-circuiting induced by sodium dendrites.<sup>[168]</sup>

## 5.2. Advanced *In-situ/In-operando* Characterization

Irreversible structural evolution during the repeated charging and discharging process, as well as material dissolution due to electrode incompatibility with other cell components, are the primary reasons for capacity degradation and short cycle life of batteries. However, the process that happens in a cell during cycling is difficult to identify with the current *ex-situ* characterization techniques. Conducting *ex-situ* characterizations require disassembling the cells which might expose its components to potential contaminants and might alter the real chemical and structural information that can be obtained. Therefore, to elucidate the real-time complex behavior, crystal structure, morphological evolution, valence state changes, and reaction mechanism of PBAs, advanced *in-situ/in-operando* techniques<sup>[71]</sup> are indispensable.

For instance, *in situ/in-operando* XRD is helpful in identifying the phase transformations and atomic occupation changes that occur during cycling.<sup>[176]</sup> With the help of *in-situ* synchrotron-based XRD (SXRD) investigations, Wang et al. revealed that the  $\text{Na}_{1.73}\text{Fe}[\text{Fe}(\text{CN})_6] \cdot 3.8\text{H}_2\text{O}$  cathode for SIBs exhibit a highly reversible three-phase transformations between rhombohedral, cubic, and tetragonal during charging and discharging, which explained the stable cycling of the material.<sup>[49]</sup> This gives a deeper understanding of the structural changes PBAs undergo and gives insight on crystal structure modulation to enable high-performance cathodes.

*In-situ* Raman Spectroscopy is capable of investigating the guest ion storage mechanism and valence state changes in real-time. Ma et al. conducted *in-situ* Raman measurements for a KIB with  $\text{K}_{1.64}\text{Fe}[\text{Fe}(\text{CN})_6]$  cathode. The *in-situ* analysis revealed that the Raman peak corresponding to  $\text{Fe}^{\text{II}}-\text{C}\equiv\text{N}$  did not disappear completely at the end of the charging process. This indicates that  $\text{K}^+$  ions were not completely extracted from its monoclinic structure, which is beneficial in terms of structural stability.<sup>[177]</sup>

*In-situ* X-ray absorption spectroscopy (XAS) can determine the chemical and electronic structure of the electrode materials in real-time. It has two regions: (1) XANES, which provides information on oxidation state, site symmetry, and electronic configuration; and (2) EXAFS, which can reveal local atomic structure, such as bond distance.<sup>[71,176]</sup> Seok et al. performed *operando* XANES (X-ray absorption near-edge structure) on SIBs with  $\text{NaFe}^{\text{III}}[\text{Fe}^{\text{II}}(\text{CN})_6]$  and  $\text{Na}_2\text{Ni}^{\text{II}}[\text{Fe}^{\text{II}}(\text{CN})_6]$  cathodes. The data from the Ni K-edge of the  $\text{Na}_2\text{Ni}^{\text{II}}[\text{Fe}^{\text{II}}(\text{CN})_6]$  indicated no significant shift in peak position across different potentials, whereas the Fe K-edge of the  $\text{NaFe}^{\text{III}}[\text{Fe}^{\text{II}}(\text{CN})_6]$  exhibited a clear gradual shift toward lower energies during discharge and higher energies during charging, demonstrating that nickel's contribution to capacity is negligible.<sup>[178]</sup> *In-situ* scanning transmission electron microscopy (STEM) with EDS mapping and electron energy loss spectroscopy (EELS) was also found to be helpful in identifying the morphological and compositional changes of PBA cathodes with varying temperatures.<sup>[179]</sup>

*In-Situ/Operando* X-ray spectroscopic imaging and tomography techniques such as X-ray computed tomography, transmission X-ray microscopy (TXM), scanning transmission X-ray microscopy (STXM), and X-ray fluorescence microscopy (XFM),

can serve as complementary methods to the previously discussed characterizations, providing different insights on a different spatial scale.<sup>[176]</sup> Overall, the knowledge gained in *in-situ/operando* techniques will help in bridging the gap between lab-scale and industrial-scale PBA-based batteries.

## 5.3. Computational Tools

In order to overcome the challenges and accelerate the development of PBA-based PLBs, computational/theoretical tools may be used to provide insights on prospective cathode candidates, elucidate mechanistic ion transport phenomena, and reduce complete dependence on experimental knowledge.<sup>[180]</sup> Several computational techniques can be employed, such as (1) first-principles calculations based on density functional theory (DFT),<sup>[47]</sup> (2) molecular dynamics (MD),<sup>[181]</sup> (3) bond valence site energy (BVSE) calculations,<sup>[182]</sup> and (4) machine learning (ML) approaches.<sup>[180]</sup>

Using DFT is a common way to gain insight on the important properties of battery materials (i.e., structural evolution, electronic structure, redox reactions, ionic diffusion). In SIBs, density of states, magnetic moment, and charge analysis were employed in DFT calculations to examine the redox processes and structural evolution of the  $\text{Na}_x\text{Fe}[\text{Fe}(\text{CN})_6]$  cathode during the desodiation process.<sup>[183]</sup> In this study, the rhombohedral phase was found to be most stable at full sodiation ( $x=2$ ); however, the structure changed to the cubic 24d phase at 50% desodiation ( $x=1$ ).<sup>[182]</sup> BVSE can be also employed to determine possible ion migration channels based on the bond valence sum of each atom in the crystal lattice.<sup>[180,184]</sup>

MD is another powerful tool in determining the dynamic behavior of materials at the molecular level through the use of Newton's equations of motion to obtain the trajectories of all atoms in the simulated system.<sup>[180,185]</sup> In the context of PBAs, MD simulations play a role in assessing and improving the properties of aqueous-based electrolytes. In 2022, Sun et al. elucidated the evolution of solvation sheaths for  $\text{Zn}^{2+}$  ions in the water-in-ethanol electrolyte using MD simulations in zinc batteries with  $\text{Na}_{1.87}\text{Mn}_{0.78}[\text{Fe}(\text{CN})_6] \cdot 2.1\text{H}_2\text{O}$  cathode.<sup>[186]</sup>

In the pursuit of accelerating material discovery that can be used for PLBs, data-driven approaches incorporating ML can be employed. ML algorithms can be trained on experimental and computational data to predict various material properties, allowing researchers to rapidly screen and discover viable candidate materials for energy storage applications.<sup>[187]</sup>

The power of the aforementioned computational techniques can be used to complement experimental knowledge in order to gain a better understanding of the structure-property-performance relationships of PBAs in PLBs.

It is critical to approach battery development from a comprehensive and holistic standpoint. While the cathode is responsible for the majority of the performance parameters, it is also necessary to investigate other components (i.e., anode, electrolyte, current collector, separator) and their compatibility with one another to develop competitive and practical next-

generation batteries with cost-effective and resource-abundant materials such as PBAs.

## Supporting Information

The authors have cited additional references within the Supporting Information.<sup>[188–220]</sup>

## Acknowledgements

This work is funded by the Department of Science and Technology (DOST) of the Philippines through the DOST-Science for Change Program (S4CP) Niche Centers in the Regions (NICER) Advanced Batteries Center (ABC) Program under the Advanced Cathode Materials for Next Generation Batteries (NextGen) Project.

## Conflict of Interests

The authors declare no conflict of interest.

**Keywords:** cathode · Prussian Blue Analogues (PBAs) · post-lithium batteries (PLBs) · rechargeable batteries · energy storage

- [1] M. Li, J. Lu, Z. Chen, K. Amine, *Adv. Mater.* **2018**, *30*, 1800561.
- [2] A. Ponrouch, M. R. Palacín, *Philos. Trans. R. Soc. Math. Phys. Eng. Sci.* **2019**, *377*, 20180297.
- [3] COM(2020) 474 final., *Critical Raw Materials Resilience: Charting a Path towards Greater Security and Sustainability*, European Commission, Brussels **2020**.
- [4] M. Fichtner, *Batteries & Supercaps* **2022**, *5*, e202100224.
- [5] J. Song, B. Xiao, Y. Lin, K. Xu, X. Li, *Adv. Energy Mater.* **2018**, *8*, 1703082.
- [6] K. C. Wasalathilake, H. Li, L. Xu, C. Yan, *J. Energy Chem.* **2020**, *42*, 91.
- [7] M. Lao, Y. Zhang, W. Luo, Q. Yan, W. Sun, S. X. Dou, *Adv. Mater.* **2017**, *29*, 1700622.
- [8] X. Wu, G. He, Y. Ding, *ChemSusChem* **2020**, *13*, 3376.
- [9] Y. Liu, G. He, H. Jiang, I. P. Parkin, P. R. Shearing, D. J. L. Brett, *Adv. Funct. Mater.* **2021**, *31*, 2010445.
- [10] A. Ponrouch, J. Bitenc, R. Dominko, N. Lindahl, P. Johansson, M. R. Palacin, *Energy Storage Mater.* **2019**, *20*, 253.
- [11] Y. Liu, R. Holze, *Encyclopedia* **2022**, *2*, 1611.
- [12] S. Chen, D. Zhao, L. Chen, G. Liu, Y. Ding, Y. Cao, Z. Chen, *Small Structures* **2021**, *2*, 2100082.
- [13] M. A. Schroeder, L. Ma, G. Pastel, K. Xu, *Curr. Opin. Electrochem.* **2021**, *29*, 100819.
- [14] G. D. D. Sanglay, J. S. Garcia, M. S. Palaganas, M. Sorolla, S. See, L. A. Limjoco, J. D. Ocon, *Molecules* **2022**, *27*, 8047.
- [15] J. Song, W. Yan, H. Cao, Q. Song, H. Ding, Z. Lv, Y. Zhang, Z. Sun, *J. Cleaner Prod.* **2019**, *215*, 570.
- [16] M. He, R. Davis, D. Chartouni, M. Johnson, M. Abplanalp, P. Troendle, R.-P. Suetterlin, *J. Power Sources* **2022**, *548*, 232036.
- [17] A. Bauer, J. Song, S. Vail, W. Pan, J. Barker, Y. Lu, *Adv. Energy Mater.* **2018**, *8*, 1702869.
- [18] CATL, “CATL Unveils Its Latest Breakthrough Technology by Releasing Its First Generation of Sodium-ion Batteries”, can be found under <https://www.catl.com/en/news/665.html>, 2021 (accessed 22 June 2024).
- [19] ALTRIS, “Altris reaches new milestone with 160 Wh/kg battery cell”, can be found under <https://www.altris.se/news/altris-reaches-new-milestone-with-160-wh/kg-battery-cell>, 2023 (accessed 22 June 2024).
- [20] HiNa Battery, “R&D achievements: Na-ion batteries”, can be found under <https://www.hinabattery.com/en/index.php?catid=15> (accessed 22 June 2024).
- [21] M. He, A. El Mejdoubi, D. Chartouni, M. Morcrette, P. Troendle, R. Castiglioni, *J. Power Sources* **2023**, *588*, 233741.
- [22] J.-M. Tarascon, *Joule* **2020**, *4*, 1616.
- [23] S. Chong, J. Yang, L. Sun, S. Guo, Y. Liu, H. K. Liu, *ACS Nano* **2020**, *14*, 9807.
- [24] M. S. Chae, J. Hyung, M. Jang, H. Lee, S.-T. Hong, *J. Power Sources* **2017**, *363*, 269.
- [25] Z. Liu, G. Pulletikurthi, F. Endres, *ACS Appl. Mater. Interfaces* **2016**, *8*, 12158.
- [26] Md. Adil, A. Sarkar, A. Roy, M. R. Panda, A. Nagendra, S. Mitra, *ACS Appl. Mater. Interfaces* **2020**, *12*, 11489.
- [27] Y. Gao, H. Yang, X. Wang, Y. Bai, N. Zhu, S. Guo, L. Suo, H. Li, H. Xu, C. Wu, *ChemSusChem* **2020**, *13*, 732.
- [28] A. K. Thakur, M. Majumder, S. P. Patole, K. Zaghib, M. V. Reddy, *Mater. Adv.* **2021**, *2*, 2457.
- [29] X. Tang, C. Liu, H. Wang, L.-P. Lv, W. Sun, Y. Wang, *Coord. Chem. Rev.* **2023**, *494*, 215361.
- [30] A. Eftekhari, *J. Power Sources* **2004**, *126*, 221.
- [31] Y. Lu, L. Wang, J. Cheng, J. B. Goodenough, *Chem. Commun.* **2012**, *48*, 6544.
- [32] H. Yi, R. Qin, S. Ding, Y. Wang, S. Li, Q. Zhao, F. Pan, *Adv. Funct. Mater.* **2021**, *31*, 2006970.
- [33] W.-J. Li, C. Han, G. Cheng, S.-L. Chou, H.-K. Liu, S.-X. Dou, *Small* **2019**, *15*, 1900470.
- [34] H. Wang, B. Deng, W. Ge, T. Chen, M. Qu, G. Peng, *Prog. Chem.* **2017**, *29*, 683.
- [35] A. Zhou, W. Cheng, W. Wang, Q. Zhao, J. Xie, W. Zhang, H. Gao, L. Xue, J. Li, *Adv. Energy Mater.* **2021**, *11*.
- [36] S. S. Kaye, J. R. Long, *Catal. Today* **2007**, *120*, 311.
- [37] Y. Lin, J. Liu, L. Shi, N. Guo, Z. Sun, C. Geng, J. Jiang, Q. Zhuang, Y. Chen, Z. Ju, *J. Colloid Interface Sci.* **2022**, *623*, 1.
- [38] B. Wang, Y. Han, X. Wang, N. Bahlawane, H. Pan, M. Yan, Y. Jiang, *iScience* **2018**, *3*, 110.
- [39] E. P. Alsaç, E. Ülker, S. V. K. Nune, Y. Dede, F. Karadas, *Chem. Eur. J.* **2018**, *24*, 4856.
- [40] K. Itaya, N. Shoji, I. Uchida, *J. Am. Chem. Soc.* **1984**, *106*, 3423.
- [41] H. Wang, H. Ohnuki, H. Endo, M. Izumi, *Sens. Actuators B* **2012**, *168*, 249.
- [42] S. Sindhu, K. Narasimha Rao, S. Ahuja, A. Kumar, E. S. R. Gopal, *Mater. Sci. Eng. B* **2006**, *132*, 39.
- [43] S. Ohkoshi, T. Iyoda, A. Fujishima, K. Hashimoto, *Phys. Rev. B* **1997**, *56*, 11642.
- [44] P. Xue, L. Sun, Q. Li, L. Zhang, Z. Xu, C. M. Li, Y. Kang, *J. Colloid Interface Sci.* **2018**, *509*, 384.
- [45] S. Ohkoshi, K. Nakagawa, M. Yoshiakiyo, A. Namai, K. Imoto, Y. Nagane, F. Jia, O. Stefanczyk, H. Tokoro, J. Wang, T. Sugahara, K. Chiba, K. Motodohi, K. Isogai, K. Nishioka, T. Momiki, R. Hatano, *Nat. Commun.* **2023**, *14*, 8466.
- [46] Y. Moritomo, Y. Yoshida, D. Inoue, H. Iwaizumi, S. Kobayashi, S. Kawaguchi, T. Shibata, *J. Phys. Soc. Jpn.* **2021**, *90*, 063801.
- [47] C. Ling, J. Chen, F. Mizuno, *J. Phys. Chem. C* **2013**, *117*, 21158.
- [48] J. Peng, J. Wang, H. Yi, W. J. Hu, Y. Yu, J. Yin, Y. Shen, Y. Liu, J. Luo, Y. Xu, P. Wei, Y. Li, Y. Jin, Y. Ding, L. Miao, J. Jiang, J. Han, Y. Huang, *Adv. Energy Mater.* **2018**, *8*.
- [49] W. Wang, Y. Gang, Z. Hu, Z. Yan, W. Li, Y. Li, Q.-F. Gu, Z. Wang, S.-L. Chou, H.-K. Liu, S.-X. Dou, *Nat. Commun.* **2020**, *11*, 980.
- [50] L. Jiang, Y. Lu, C. Zhao, L. Liu, J. Zhang, Q. Zhang, X. Shen, J. Zhao, X. Yu, H. Li, X. Huang, L. Chen, Y.-S. Hu, *Nat. Energy* **2019**, *4*, 495.
- [51] Y. Gao, Y. Huang, H. Pan, L. Ji, L. Wang, Y. Tang, Y. Zhu, M. Yan, G. Sun, W. Ni, Y. Jiang, *J. Alloys Compd.* **2023**, *950*, 169886.
- [52] X. Liu, H. Gong, C. Han, Y. Cao, Y. Li, J. Sun, *Energy Storage Mater.* **2023**, *57*, 118.
- [53] N. Imanishi, T. Morikawa, J. Kondo, Y. Takeda, O. Yamamoto, N. Kinugasa, T. Yamagishi, *J. Power Sources* **1999**, *79*, 215.
- [54] Y. Mizuno, M. Okubo, E. Hosono, T. Kudo, K. Ohishi, A. Okazawa, N. Kojima, R. Kurono, S. Nishimura, A. Yamada, *J. Mater. Chem. A* **2013**, *1*, 13055.
- [55] A. L. Lipson, B. Pan, S. H. Lapidus, C. Liao, J. T. Vaughney, B. J. Ingram, *Chem. Mater.* **2015**, *27*, 8442.
- [56] L. Zhang, L. Chen, X. Zhou, Z. Liu, *Adv. Energy Mater.* **2015**, *5*, 1400930.
- [57] S. Liu, G. L. Pan, G. R. Li, X. P. Gao, *J. Mater. Chem. A* **2014**, *3*, 959.

- [58] X. Wu, C. Wu, C. Wei, L. Hu, J. Qian, Y. Cao, X. Ai, J. Wang, H. Yang, *ACS Appl. Mater. Interfaces* **2016**, *8*, 5393.
- [59] Y. Li, Q. Dang, W. Chen, L. Tang, M. Hu, *J. Inorg. Organomet. Polym. Mater.* **2021**, *31*, 1877.
- [60] J.-H. Lee, G. Ali, D. H. Kim, K. Y. Chung, *Adv. Energy Mater.* **2017**, *7*, 1601491.
- [61] S. Xu, Y. Wang, L. Ben, Y. Lyu, N. Song, Z. Yang, Y. Li, L. Mu, H.-T. Yang, L. Gu, Y.-S. Hu, H. Li, Z.-H. Cheng, L. Chen, X. Huang, *Adv. Energy Mater.* **2015**, *5*, 1501156.
- [62] B. Xie, B. Sun, T. Gao, Y. Ma, G. Yin, P. Zuo, *Coord. Chem. Rev.* **2022**, *460*, 214478.
- [63] M. Cao, X. Wu, X. He, C. Hu, *Chem. Commun.* **2005**, 2241.
- [64] H. Ming, N. L. K. Torad, Y.-D. Chiang, K. C.-W. Wu, Y. Yamauchi, *CrystEngComm* **2012**, *14*, 3387.
- [65] S. He, J. Zhao, X. Rong, C. Xu, Q. Zhang, X. Shen, X. Qi, Y. Li, X. Li, Y. Niu, X. Li, S. Han, L. Gu, H. Liu, Y.-S. Hu, *Chem. Eng. J.* **2022**, *428*, 131083.
- [66] F. Qu, A. Shi, M. Yang, J. Jiang, G. Shen, R. Yu, *Anal. Chim. Acta* **2007**, *605*, 28.
- [67] P. Zhou, D. Xue, H. Luo, X. Chen, *Nano Lett.* **2002**, *2*, 845.
- [68] A. Johansson, E. Widenkvist, J. Lu, M. Boman, U. Jansson, *Nano Lett.* **2005**, *5*, 1603.
- [69] J. Qian, C. Wu, Y. Cao, Z. Ma, Y. Huang, X. Ai, H. Yang, *Adv. Energy Mater.* **2018**, *8*.
- [70] X. Wu, M. Sun, S. Guo, J. Qian, Y. Liu, Y. Cao, X. Ai, H. Yang, *ChemNanoMat* **2015**, *1*, 188.
- [71] X.-H. Liu, J. Peng, W.-H. Lai, Y. Gao, H. Zhang, L. Li, Y. Qiao, S.-L. Chou, *Adv. Funct. Mater.* **2022**, *32*, 2108616.
- [72] Y. Yang, J. Zhou, L. Wang, Z. Jiao, M. Xiao, Q. Huang, M. Liu, Q. Shao, X. Sun, J. Zhang, *Nano Energy* **2022**, *99*, 107424.
- [73] P. K. Nayak, L. Yang, W. Brehm, P. Adelhelm, *Angew. Chem. Int. Ed.* **2018**, *57*, 102.
- [74] K. Kubota, S. Komaba, *J. Electrochem. Soc.* **2015**, *162*, A2538.
- [75] P. Gupta, S. Pushpakant, M. A. Haider, S. Basu, *ACS Omega* **2022**, *7*, 5605.
- [76] Y. Tang, W. Li, P. Feng, M. Zhou, K. Wang, Y. Wang, K. Zaghib, K. Jiang, *Adv. Funct. Mater.* **2020**, *30*, 1908754.
- [77] M. Takachi, T. Matsuda, Y. Moritomo, *Appl. Phys. Express* **2013**, *6*, 025802.
- [78] B. Wang, X. Wang, C. Liang, M. Yan, Y. Jiang, *ChemElectroChem* **2019**, *6*, 4848.
- [79] D. J. Kim, Y. H. Jung, K. K. Bharathi, S. H. Je, D. K. Kim, A. Coskun, J. W. Choi, *Adv. Energy Mater.* **2014**, *4*, 1400133.
- [80] Y. Lin, B. Han, D. Zhang, X. Liu, Z. Wang, Z. Wang, L. Si, S. Zhang, C. Deng, *J. Energy Chem.* **2022**, *74*, 72.
- [81] X. Ma, J. Chen, C. Yu, J. Sun, X. Cao, Z. Cheng, Y. Guo, X. Wang, Z. Zi, J. Dai, *J. Electroanal. Chem.* **2022**, *918*, 116468.
- [82] Y. Sun, C. Liu, J. Xie, D. Zhuang, W. Zheng, X. Zhao, *New J. Chem.* **2019**, *43*, 11618.
- [83] T. Hosaka, K. Kubota, A. S. Hameed, S. Komaba, *Chem. Rev.* **2020**, *120*, 6358.
- [84] C. Liu, J. Ma, *J. Alloys Compd.* **2023**, *942*, 169127.
- [85] Q. Xue, L. Li, Y. Huang, R. Huang, F. Wu, R. Chen, *ACS Appl. Mater. Interfaces* **2019**, *11*, 22339.
- [86] X. Jiang, T. Zhang, L. Yang, G. Li, J. Y. Lee, *ChemElectroChem* **2017**, *4*, 2237.
- [87] S. Lee, J. Cho, *Angew. Chem. Int. Ed.* **2015**, *54*, 9452.
- [88] H. Tang, Z. Peng, L. Wu, F. Xiong, C. Pei, Q. An, L. Mai, *Electrochem. Energy Rev.* **2018**, *1*, 169.
- [89] F. Ma, Q. Li, T. Wang, H. Zhang, G. Wu, *Sci. Bull.* **2017**, *62*, 358.
- [90] D. Selvakumaran, A. Pan, S. Liang, G. Cao, *J. Mater. Chem. A* **2019**, *7*, 18209.
- [91] R. Guduru, J. Icaza, *Nanomaterials* **2016**, *6*, 41.
- [92] Y. Zhang, J. Cao, Z. Yuan, H. Xu, D. Li, Y. Li, W. Han, L. Wang, *Small* **2022**, *18*, 2202313.
- [93] M. Guo, C. Yuan, T. Zhang, X. Yu, *Small* **2022**, *18*, 2106981.
- [94] S. Yagi, M. Fukuda, T. Ichitsubo, K. Nitta, M. Mizumaki, E. Matsubara, *J. Electrochem. Soc.* **2015**, *162*, A2356.
- [95] D. Wang, X. Gao, Y. Chen, L. Jin, C. Kuss, P. G. Bruce, *Nat. Mater.* **2018**, *17*, 16.
- [96] R. J. Gummow, G. Vamvounis, M. B. Kannan, Y. He, *Adv. Mater.* **2018**, *30*, 1801702.
- [97] R. Y. Wang, C. D. Wessells, R. A. Huggins, Y. Cui, *Nano Lett.* **2013**, *13*, 5748.
- [98] A. L. Lipson, S.-D. Han, S. Kim, B. Pan, N. Sa, C. Liao, T. T. Fister, A. K. Burrell, J. T. Vaughey, B. J. Ingram, *J. Power Sources* **2016**, *325*, 646.
- [99] T. Tojo, Y. Sugiura, R. Inada, Y. Sakurai, *Electrochim. Acta* **2016**, *207*, 22.
- [100] Md. Adil, P. K. Dutta, S. Mitra, *ChemistrySelect* **2018**, *3*, 3687.
- [101] P. Padigi, N. Kuperman, J. J. Thiebes, G. Goncher, D. Evans, R. Solanki, *J. New Mater. Electrochem. Syst.* **2016**, *19*, 057.
- [102] L. Chen, Q. An, L. Mai, *Adv. Mater. Interfaces* **2019**, *6*, 1900387.
- [103] L.-P. Wang, P.-F. Wang, T.-S. Wang, Y.-X. Yin, Y.-G. Guo, C.-R. Wang, *J. Power Sources* **2017**, *355*, 18.
- [104] Z. Liu, P. Bertram, F. Endres, *J. Solid State Electrochem.* **2017**, *21*, 2021.
- [105] L. Ma, S. Chen, C. Long, X. Li, Y. Zhao, Z. Liu, Z. Huang, B. Dong, J. A. Zapien, C. Zhi, *Adv. Energy Mater.* **2019**, *9*, 1902446.
- [106] Z. Hou, X. Zhang, X. Li, Y. Zhu, J. Liang, Y. Qian, *J. Mater. Chem. A* **2017**, *5*, 730.
- [107] L. D. Reed, S. N. Ortiz, M. Xiong, E. J. Menke, *Chem. Commun.* **2015**, *51*, 14397.
- [108] C. Li, X. Wang, W. Deng, C. Liu, J. Chen, R. Li, M. Xue, *ChemElectroChem* **2018**, *5*, 3887.
- [109] G. Du, H. Pang, *Energy Storage Mater.* **2021**, *36*, 387.
- [110] C. Yan, A. Zhao, F. Zhong, X. Feng, W. Chen, J. Qian, X. Ai, H. Yang, Y. Cao, *Electrochim. Acta* **2020**, *332*, 135533.
- [111] J. Peng, W. Zhang, Z. Hu, L. Zhao, C. Wu, G. Peleckis, Q. Gu, J.-Z. Wang, H. K. Liu, S. X. Dou, S. Chou, *Nano Lett.* **2022**, *22*, 1302.
- [112] A. Mullalui, M. Gaboardi, J. R. Plaisier, S. Passerini, M. Giorgetti, *ACS Appl. Energ. Mater.* **2020**, *3*, 5728.
- [113] R. Rehman, J. Peng, H. Yi, Y. Shen, J. Yin, C. Li, C. Fang, Q. Li, J. Han, *RSC Adv.* **2020**, *10*, 27033.
- [114] D. A. El-Hady, Y. Lyu, S. Zhan, J. Yang, Y. Wang, F. Yang, Q. Zhao, M. Gu, M. Shao, *ACS Appl. Energ. Mater.* **2022**, *5*, 8547.
- [115] W. Shu, M. Huang, L. Geng, F. Qiao, X. Wang, *Small* **2023**, *19*, 2207080.
- [116] Y. Liu, G. Wei, M. Ma, Y. Qiao, *Chem. Eur. J.* **2017**, *23*, 15991.
- [117] T. Cao, F. Zhang, M. Chen, T. Shao, Z. Li, Q. Xu, D. Cheng, H. Liu, Y. Xia, *ACS Appl. Mater. Interfaces* **2021**, *13*, 26924.
- [118] W.-J. Li, S.-L. Chou, J.-Z. Wang, Y.-M. Kang, J.-L. Wang, Y. Liu, Q.-F. Gu, H.-K. Liu, S.-X. Dou, *Chem. Mater.* **2015**, *27*, 1997.
- [119] S. Yu, Y. Li, Y. Lu, B. Xu, Q. Wang, M. Yan, Y. Jiang, *J. Power Sources* **2015**, *275*, 45.
- [120] H. Fu, C. Liu, C. Zhang, W. Ma, K. Wang, Z. Li, X. Lu, G. Cao, *J. Mater. Chem. A* **2017**, *5*, 9604.
- [121] B. Huang, Y. Shao, Y. Liu, Z. Lu, X. Lu, S. Liao, *ACS Appl. Energ. Mater.* **2019**, *2*, 6528.
- [122] H. Zhang, J. Peng, L. Li, Y. Zhao, Y. Gao, J. Wang, Y. Cao, S. Dou, S. Chou, *Adv. Funct. Mater.* **2023**, *33*, 2210725.
- [123] L.-L. Zhang, Z.-Y. Chen, X.-Y. Fu, B. Yan, H.-C. Tao, X.-L. Yang, *Chem. Eng. J.* **2022**, *433*, 133739.
- [124] J. Kim, S.-H. Yi, L. Li, S.-E. Chun, *J. Energy Chem.* **2022**, *69*, 649.
- [125] Z.-Y. Chen, X.-Y. Fu, L.-L. Zhang, B. Yan, X.-L. Yang, *ACS Appl. Mater. Interfaces* **2022**, *14*, 5506.
- [126] Y. Ma, Y. Ma, S. L. Dreyer, Q. Wang, K. Wang, D. Goonetilleke, A. Omar, D. Mikhailova, H. Hahn, B. Breitung, T. Brezesinski, *Adv. Mater.* **2021**, *33*, 2101342.
- [127] S. Jeon, C. H. Li, D. R. Talham, *Cryst. Growth Des.* **2021**, *21*, 916.
- [128] P. Hu, W. Peng, B. Wang, D. Xiao, U. Ahuja, J. Réthoré, K. E. Aifantis, *ACS Energy Lett.* **2020**, *5*, 100.
- [129] B. Wang, Y. Han, Y. Chen, Y. Xu, H. Pan, W. Sun, S. Liu, M. Yan, Y. Jiang, *J. Mater. Chem. A* **2018**, *6*, 8947.
- [130] H. Wang, Q. Zhu, H. Li, C. Xie, D. Zeng, *Cryst. Growth Des.* **2018**, *18*, 5780.
- [131] J. Nai, X. W. (David) Lou, *Adv. Mater.* **2019**, *31*, 1706825.
- [132] Y. Luo, J. Peng, Y. Yan, *RSC Adv.* **2021**, *11*, 31827.
- [133] F. Feng, S. Chen, X.-Z. Liao, Z.-F. Ma, *Small Methods* **2019**, *3*, 1800259.
- [134] Y. Zeng, J. Xu, Y. Wang, S. Li, D. Luan, X. W. (David) Lou, *Angew. Chem. Int. Ed.* **2022**, *61*, e202212031.
- [135] Y. Zeng, X. F. Lu, S. L. Zhang, D. Luan, S. Li, X. W. (David) Lou, *Angew. Chem. Int. Ed.* **2021**, *60*, 22189.
- [136] W. Gong, M. Wan, R. Zeng, Z. Rao, S. Su, L. Xue, W. Zhang, Y. Huang, *Energy Technol.* **2019**, *7*, 1900108.
- [137] C. H. Li, Y. Nanba, D. Asakura, M. Okubo, D. R. Talham, *RSC Adv.* **2014**, *4*, 24955.
- [138] Y. Wei, M. Zheng, W. Zhu, H. Pang, *Carbon Neutralization* **2023**, *2*, 271.

- [139] T. Hosaka, T. Fukabori, H. Kojima, K. Kubota, S. Komaba, *ChemSusChem* **2021**, *14*, 1166.
- [140] T. Huang, Y. Niu, Q. Yang, W. Yang, M. Xu, *ACS Appl. Mater. Interfaces* **2021**, *13*, 37187.
- [141] Y. Ruan, L. Chen, L. Cui, Q. An, *Coating* **2022**, *12*, 779.
- [142] Z. Wang, Y. Huang, D. Chu, C. Li, Y. Zhang, F. Wu, L. Li, M. Xie, J. Huang, R. Chen, *ACS Appl. Mater. Interfaces* **2021**, *13*, 38202.
- [143] J. Peng, W. Zhang, Q. Liu, J. Wang, S. Chou, H. Liu, S. Dou, *Adv. Mater.* **2022**, *34*, 2108384.
- [144] B. Tang, X. Yu, Y. Gao, S.-H. Bo, Z. Zhou, *Sci. Bull.* **2022**, *67*, 2149.
- [145] ACS Chemical and Engineering News (C&EN), "Start-up Group1 seeks to commercialize potassium-ion batteries", can be found under <https://cen.acs.org/energy/energy-storage-/Start-up-Group1-seeks-commercialize-potassium-ion/100/web/2022/07> (accessed 22 June 2024).
- [146] L. Wang, Y. Lu, J. Liu, M. Xu, J. Cheng, D. Zhang, J. B. Goodenough, *Angew. Chem. Int. Ed.* **2013**, *52*, 1964.
- [147] Z. Xu, Y. Sun, J. Xie, Y. Nie, X. Xu, J. Tu, J. Zhang, L. Qiu, T. Zhu, X. Zhao, *ACS Sustainable Chem. Eng.* **2022**, *10*, 13277.
- [148] Benchmark, "Sodium Ion Batteries 101: Their Promise and Future", can be found under <https://source.benchmarkminerals.com/downloads/special-issues/1317717> (accessed 22 June 2024).
- [149] L. Wang, J. Song, R. Qiao, L. A. Wray, M. A. Hossain, Y.-D. Chuang, W. Yang, Y. Lu, D. Evans, J.-J. Lee, S. Vail, X. Zhao, M. Nishijima, S. Kakimoto, J. B. Goodenough, *J. Am. Chem. Soc.* **2015**, *137*, 2548.
- [150] Y. E. Durmus, H. Zhang, F. Baakes, G. Desmaizieres, H. Hayun, L. Yang, M. Kolek, V. Küpers, J. Janek, D. Mandler, S. Passerini, Y. Ein-Eli, *Adv. Energy Mater.* **2020**, *10*, 2000089.
- [151] Z. Yang, J. Zhang, M. C. W. Kintner-Meyer, X. Lu, D. Choi, J. P. Lemmon, J. Liu, *Chem. Rev.* **2011**, *111*, 3577.
- [152] Q. Wang, B. Jiang, B. Li, Y. Yan, *Renewable Sustainable Energy Rev.* **2016**, *64*, 106.
- [153] R. Zhang, B. Xia, B. Li, L. Cao, Y. Lai, W. Zheng, H. Wang, W. Wang, *Energies* **2018**, *11*, 1820.
- [154] G. L. Soloveichik, *Annu. Rev. Chem. Biomol. Eng.* **2011**, *2*, 503.
- [155] N. Opiyo, *J. Energy Storage* **2016**, *7*, 1.
- [156] M. A. Fetcenko, S. R. Ovshinsky, B. Reichman, K. Young, C. Fierro, J. Koch, A. Zallen, W. Mays, T. Ouchi, *J. Power Sources* **2007**, *165*, 544.
- [157] D. Kumar, S. K. Rajouria, S. B. Kuhar, D. K. Kanchan, *Solid State Ionics* **2017**, *312*, 8.
- [158] K. B. Hueso, M. Armand, T. Rojo, *Energy Environ. Sci.* **2013**, *6*, 734.
- [159] H. Liu, X. Cheng, Y. Chong, H. Yuan, J.-Q. Huang, Q. Zhang, *Particuology* **2021**, *57*, 56.
- [160] A. Väyrynen, J. Salminen, *J. Chem. Thermodyn.* **2012**, *46*, 80.
- [161] J. Smeekens, R. Gopalakrishnan, N. V. den Steen, N. Omar, O. Hegazy, A. Hubin, J. Van Mierlo, *Energies* **2016**, *9*, 104.
- [162] W. Wang, Y. Gang, J. Peng, Z. Hu, Z. Yan, W. Lai, Y. Zhu, D. Appadoo, M. Ye, Y. Cao, Q.-F. Gu, H.-K. Liu, S.-X. Dou, S.-L. Chou, *Adv. Funct. Mater.* **2022**, *32*, 2111727.
- [163] Y. Xu, J. Wan, L. Huang, M. Ou, C. Fan, P. Wei, J. Peng, Y. Liu, Y. Qiu, X. Sun, C. Fang, Q. Li, J. Han, Y. Huang, J. A. Alonso, Y. Zhao, *Adv. Energy Mater.* **2019**, *9*, 1803158.
- [164] J. Wang, L. Li, S. Zuo, Y. Zhang, L. Lv, R. Ran, X. Li, B. Li, F. Zhao, J. Zhang, Y. Wang, P. Nie, *Electrochim. Acta* **2020**, *341*, 136057.
- [165] Q. Liu, Z. Hu, M. Chen, C. Zou, H. Jin, S. Wang, S.-L. Chou, Y. Liu, S.-X. Dou, *Adv. Funct. Mater.* **2020**, *30*.
- [166] P. Yadav, A. Patrike, K. Wasnik, V. Shelke, M. Shelke, *Mater. Today Sustain.* **2023**, *22*, 100385.
- [167] W. Shu, C. Han, X. Wang, *Adv. Funct. Mater.* **2024**, *34*, 2309636.
- [168] G. Du, M. Tao, J. Li, T. Yang, W. Gao, J. Deng, Y. Qi, S.-J. Bao, M. Xu, *Adv. Energy Mater.* **2020**, *10*, 1903351.
- [169] S. Wheeler, I. Capone, S. Day, C. Tang, M. Pasta, *Chem. Mater.* **2019**, *31*, 2619.
- [170] T. Shiga, H. Kondo, Y. Kato, M. Inoue, *J. Phys. Chem. C* **2015**, *119*, 27946.
- [171] K. Nakamoto, R. Sakamoto, Y. Sawada, M. Ito, S. Okada, *Small Methods* **2019**, *3*, 1800220.
- [172] A. Zhou, L. Jiang, J. Yue, Y. Tong, Q. Zhang, Z. Lin, B. Liu, C. Wu, L. Suo, Y.-S. Hu, H. Li, L. Chen, *ACS Appl. Mater. Interfaces* **2019**, *11*, 41356.
- [173] D. R. MacFarlane, N. Tachikawa, M. Forsyth, J. M. Pringle, P. C. Howlett, G. D. Elliott, J. H. Davis, M. Watanabe, P. Simon, C. A. Angell, *Energy Environ. Sci.* **2013**, *7*, 232.
- [174] M. Fiore, S. Wheeler, K. Hurlbutt, I. Capone, J. Fawdon, R. Ruffo, M. Pasta, *Chem. Mater.* **2020**, *32*, 7653.
- [175] B. Xie, L. Wang, H. Li, H. Huo, C. Cui, B. Sun, Y. Ma, J. Wang, G. Yin, P. Zuo, *Energy Storage Mater.* **2021**, *36*, 99.
- [176] D. Hou, D. Xia, E. Gabriel, J. A. Russell, K. Graff, Y. Ren, C.-J. Sun, F. Lin, Y. Liu, H. Xiong, *ACS Energy Lett.* **2021**, *6*, 4023.
- [177] R. Ma, Z. Wang, Q. Fu, W. Zhou, Y. Mo, J. Tu, Z. Wang, P. Gao, C. Fan, J. Liu, *J. Energy Chem.* **2023**, *83*, 16.
- [178] J. Seok, S.-H. Yu, H. D. Abruna, *J. Phys. Chem. C* **2020**, *124*, 16332.
- [179] Z. Li, M. Dadsetan, J. Gao, S. Zhang, L. Cai, A. Naseri, M. E. Jimenez-Castaneda, T. Filley, J. T. Miller, M. J. Thomson, V. G. Pol, *Adv. Energy Mater.* **2021**, *11*, 2101764.
- [180] M. H. Alfaruqi, S. Lee, H. Kang, B. Sambandam, V. Mathew, J.-Y. Hwang, J. Kim, *J. Phys. Chem. C* **2022**, *126*, 9209.
- [181] L. Chen, W. Sun, K. Xu, Q. Dong, L. Zheng, J. Wang, D. Lu, Y. Shen, J. Zhang, F. Fu, H. Kong, J. Qin, H. Chen, *ACS Energy Lett.* **2022**, *7*, 1672.
- [182] S. J. R. Prabakar, W.-B. Park, J. Y. Seo, S. P. Singh, D. Ahn, K.-S. Sohn, M. Pyo, *Energy Storage Mater.* **2021**, *43*, 85.
- [183] Y. P. Wang, B. P. Hou, X. R. Cao, S. Q. Wu, Z. Z. Zhu, *J. Electrochem. Soc.* **2022**, *169*, 010525.
- [184] Y. Pu, R. Dai, S. Adams, *Phys. Status Solidi A* **2021**, *218*, 2100318.
- [185] L. Zeng, J. Peng, J. Zhang, X. Tan, X. Ji, S. Li, G. Feng, *J. Chem. Phys.* **2023**, *159*, 091001.
- [186] Y. Sun, Z. Xu, X. Xu, Y. Nie, J. Tu, A. Zhou, J. Zhang, L. Qiu, F. Chen, J. Xie, T. Zhu, X. Zhao, *Energy Storage Mater.* **2022**, *48*, 192.
- [187] L. Zhou, A. M. Yao, Y. Wu, Z. Hu, Y. Huang, Z. Hong, *Adv. Theory Simul.* **2021**, *4*, 2100196.
- [188] X.-G. Yang, T. Liu, C.-Y. Wang, *Nat. Energy* **2021**, *6*, 176.
- [189] S. Kothari, "BYD Blade Battery: Everything You Should Know [Update]", can be found under <https://topelectricsuv.com/news/byd/byd-blade-battery-update/>, 2022 (accessed 22 June 2024).
- [190] EVE Battery, "Specifications: LF280 K", can be found under [https://www.evermall.eu/goods/LF280\\_K](https://www.evermall.eu/goods/LF280_K) (accessed 22 June 2024).
- [191] Pylon Technologies Co., Ltd., "Pylontech PF25 N Specifications Sheet", can be found under [https://en.pylontech.com.cn/view\\_pdf/web-viewer.html?file=/A\\_Upload/upload\\_file/20200723054014897.pdf&fname=Energy+cell+spec..pdf.pdf](https://en.pylontech.com.cn/view_pdf/web-viewer.html?file=/A_Upload/upload_file/20200723054014897.pdf&fname=Energy+cell+spec..pdf.pdf) (accessed 22 June 2024).
- [192] T. M. M. Heenan, A. Jnawali, M. Kok, T. G. Tranter, C. Tan, A. Dimitrijevic, R. Jervis, D. J. L. Brett, P. R. Shearing, *Data Brief* **2020**, *32*, 106033.
- [193] Z. Wang, J. Yuan, X. Zhu, H. Wang, L. Huang, Y. Wang, S. Xu, J. *Energy Chem.* **2021**, *55*, 484.
- [194] K. S. Oh, "Product Specification: Rechargeable Lithium-Ion Battery Model: INR18650 MJ1 3500mAh", can be found under <https://www.nkon.nl/sk/k/Specification%20INR18650MJ1%202022.08.2014.pdf>, 2014 (accessed 22 June 2024).
- [195] F. C. Krause, J. A. Loveland, M. C. Smart, E. J. Brandon, R. V. Bugga, *J. Power Sources* **2020**, *449*, 227544.
- [196] Panasonic, "Specifications Sheet: NCR-18650B", can be found under [https://www.imrbatteries.com/content/panasonic\\_ncr18650b-2.pdf](https://www.imrbatteries.com/content/panasonic_ncr18650b-2.pdf) (accessed 22 June 2024).
- [197] Q. Yang, W. Wang, H. Li, J. Zhang, F. Kang, B. Li, *Electrochim. Acta* **2018**, *270*, 96.
- [198] C. Q. X. Lim, Z.-K. Tan, *ACS Appl. Energ. Mater.* **2021**, *4*, 6214.
- [199] K. Nakamoto, R. Sakamoto, M. Ito, A. Kitajou, S. Okada, *Electrochemistry* **2017**, *85*, 179.
- [200] H.-W. Lee, R. Y. Wang, M. Pasta, S. Woo Lee, N. Liu, Y. Cui, *Nat. Commun.* **2014**, *5*, 5280.
- [201] Z. Jia, J. Wang, Y. Wang, *RSC Adv.* **2014**, *4*, 22768.
- [202] Md. Adil, S. Sau, P. Dammala, S. Mitra, *Energy Fuels* **2022**, *36*, 7816.
- [203] Y. Xu, J. Wan, L. Huang, J. Xu, M. Ou, Y. Liu, X. Sun, S. Li, C. Fang, Q. Li, J. Han, Y. Huang, Y. Zhao, *Energy Storage Mater.* **2020**, *33*, 432.
- [204] Z. Ji, B. Han, H. Liang, C. Zhou, Q. Gao, K. Xia, J. Wu, *ACS Appl. Mater. Interfaces* **2016**, *8*, 33619.
- [205] D. Yang, J. Xu, X.-Z. Liao, Y.-S. He, H. Liu, Z.-F. Ma, *Chem. Commun.* **2014**, *50*, 13377.
- [206] D.-M. Kim, Y. Kim, D. Arumugam, S. W. Woo, Y. N. Jo, M.-S. Park, Y.-J. Kim, N.-S. Choi, K. T. Lee, *ACS Appl. Mater. Interfaces* **2016**, *8*, 8554.
- [207] X. Sun, V. Duffort, L. F. Nazar, *Adv. Sci.* **2016**, *3*, 1600044.
- [208] H. Dong, Y. Li, Y. Liang, G. Li, C.-J. Sun, Y. Ren, Y. Lu, Y. Yao, *Chem. Commun.* **2016**, *52*, 8263.
- [209] L. Chen, J. L. Bao, X. Dong, D. G. Truhlar, Y. Wang, C. Wang, Y. Xia, *ACS Energy Lett.* **2017**, *2*, 1115.
- [210] C. Lee, S.-K. Jeong, *Electrochim. Acta* **2018**, *265*, 430.
- [211] C. Lee, S.-K. Jeong, *Chem. Lett.* **2016**, *45*, 1447.
- [212] C. Lee, S.-K. Jeong, *Electrochemistry* **2018**, *86*, 134.
- [213] N. Kuperman, P. Padigi, G. Goncher, D. Evans, J. Thiebes, R. Solanki, *J. Power Sources* **2017**, *342*, 414.
- [214] P. Padigi, G. Goncher, D. Evans, R. Solanki, *J. Power Sources* **2015**, *273*, 460.

- [215] G. Kasiri, R. Trócoli, A. Bani Hashemi, F. La Mantia, *Electrochim. Acta* **2016**, 222, 74.
- [216] V. Renman, D. O. Ojwang, M. Valvo, C. P. Gómez, T. Gustafsson, G. Svensson, *J. Power Sources* **2017**, 369, 146.
- [217] T. Gupta, A. Kim, S. Phadke, S. Biswas, T. Luong, B. J. Hertzberg, M. Chamoun, K. Evans-Lutterodt, D.A. Steingart, *J. Power Sources* **2016**, 305, 22.
- [218] M. S. Chae, J. W. Heo, H. H. Kwak, H. Lee, S.-T. Hong, *J. Power Sources* **2017**, 337, 204.
- [219] D. Zhang, Z. Yang, J. Zhang, H. Mao, J. Yang, Y. Qian, *J. Power Sources* **2018**, 399, 1.
- [220] Y. Ru, S. Zheng, H. Xue, H. Pang, *Chem. Eng. J.* **2020**, 382, 122853.

---

Manuscript received: April 24, 2024  
Revised manuscript received: June 29, 2024  
Accepted manuscript online: July 7, 2024  
Version of record online: August 30, 2024

---